

# Characterization of AGN and their hosts in the Extended Groth Strip: a multiwavelength analysis.

C. Ramos Almeida<sup>1</sup>, J.M. Rodríguez Espinosa<sup>1</sup>, G. Barro<sup>2</sup>, J. Gallego<sup>2</sup>, and P. G. Pérez-González<sup>2,3</sup>

## ABSTRACT

We have employed a reliable technique of classification of Active Galactic Nuclei (AGN) based on the fit of well-sampled spectral energy distributions (SEDs) with a complete set of AGN and starburst galaxy templates. We have compiled ultraviolet, optical, and infrared data for a sample of 116 AGN originally selected for their X-ray and mid-infrared emissions (96 with single detections and 20 with double optical counterparts). This is the most complete compilation of multiwavelength data for such a big sample of AGN in the Extended Groth Strip (EGS). Through these SEDs, we are able to obtain highly reliable photometric redshifts and to distinguish between pure and host-dominated AGN. For the objects with unique detection we find that they can be separated into five main groups, namely: *Starburst-dominated AGN* (24 % of the sample), *Starburst-contaminated AGN* (7 %), *Type-1 AGN* (21 %), *Type-2 AGN* (24 %), and *Normal galaxy hosting AGN* (24 %). We find these groups concentrated at different redshifts: *Type-2 AGN* and *Normal galaxy hosting AGN* are concentrated at low redshifts, whereas *Starburst-dominated AGN* and *Type-1 AGN* show a larger span. Correlations between hard/soft X-ray and ultraviolet, optical and infrared luminosities, respectively, are reported for the first time for such a sample of AGN spanning a wide range of redshifts. For the 20 objects with double detection the percentage of *Starburst-dominated AGN* increases up to 48%.

*Subject headings:* galaxies:active - galaxies:nuclei - galaxies:starburst - ultraviolet:galaxies - infrared:galaxies - X-rays:galaxies

---

<sup>1</sup>Instituto de Astrofísica de Canarias (IAC), C/Vía Láctea, s/n, E-38205, La Laguna, Tenerife, Spain. cra@iac.es and jre@iac.es

<sup>2</sup>Departamento de Astrofísica y Ciencias de la Atmósfera, Facultad de Ciencias Físicas, Universidad Complutense de Madrid, E-28040 Madrid, Spain. gbc@astrax.fis.ucm.es, jgm@astrax.fis.ucm.es, and pg-perez@astrax.fis.ucm.es

<sup>3</sup>Associate Astronomer at Steward Observatory, University of Arizona, Tucson, AZ 85721.

## 1. Introduction

The role of AGN in the formation and evolution of galaxies is still not well established. It is not clear whether AGN represent episodic phenomena in the life of galaxies, are random processes (given that the Supermassive Black Hole is already there), or are more fundamental. Some authors claim that AGN are key in quenching the star formation bursts in their host galaxies (Granato et al. 2004; Springel et al. 2005). It has also been shown that the mass dependence of the peak star-formation epoch appears to mirror the mass dependence of Black Hole (BH) activity, as recently seen in redshift surveys of both radio- and X-ray-selected active galactic nuclei (Waddington et al. 2001; Hasinger 2003b). For these reasons, searching for signatures of AGN feedback in the properties of AGN host galaxies is one of the most promising ways of testing the role of AGN in galaxy evolution.

One way of finding variations in the AGN population with redshift is to compare their SEDs defined over a broad wavelength range. The SED of an AGN can reveal the presence of the underlying central engine, together with the luminosity of the host galaxy, the reddening, and the role of the star formation in the various frequency regimes. SED determination in samples of AGN at different redshifts is an efficient method to search for evolutionary trends. Accuracy in the photometry and a filter set spanning a broad wavelength range are required to characterize correctly different types of AGN.

Multiwavelength surveys are fundamental in the study of active galactic nuclei, since these appear considerably different depending on the wavelength range of consideration. The hard X-ray selection of AGN using deep observations is one of the most reliable methods of finding AGN (Mushotzky 2004), although a percentage of them remains undetected using this technique (Peterson et al. 2006), specially the most highly obscured objects. For this reason, it is important to characterize AGN at different wavelength ranges, in order to be capable of identifying them by more than one selection technique, and to distinguish between the different groups of active nuclei, including those that could be contaminated, or even hidden, by starbursts. Mid-infrared surveys have been very successful in finding X-ray undetected AGN in large numbers, but in this case it is crucial to distinguish the AGN from the non-active star-forming galaxies. This can be achieved using typical mid-infrared colors of AGN (Lacy et al. 2004; Stern et al. 2005; Alonso-Herrero et al. 2006; Donley et al. 2008) or by combining mid-infrared and radio detections (Donley et al. 2005; Alonso-Herrero et al. 2006; Martínez-Sansigre et al. 2005, 2007; Lacy et al. 2007; Park et al. 2008).

The Extended Groth Strip ( $\alpha = 14^h 17^m$ ,  $\delta = 52^\circ 30'$ ) enlarges the Hubble Space Telescope Groth-Westphal strip (Groth et al. 1994) up to  $2^\circ \times 15'$ , having the advantage of being a low extinction area in the northern sky, with low galactic and zodiacal infrared emission, and good schedulability by space observatories. For these reasons, there is a huge

amount of public data at different wavelength ranges that only require to be compiled and cross-correlated in a consistent way. The overall majority of the observational work in the EGS have been coordinated by the AEGIS project<sup>1</sup> (Davis et al. 2007).

With the huge amount of data available for this region of the sky, we have constructed a robust AGN sample, detected in the X-rays and in the mid-infrared, intermediate in depth and area in comparison with other surveys (Jannuzi & Dey 1999; Dickinson et al. 2001; Lonsdale et al. 2003; Eisenhardt et al. 2004; Franceschini et al. 2005). The photometry has been performed over the publicly available images, in several bands, in order to compile as best-sampled SEDs as possible. The biggest advantage of our AGN sample, compared with other works, is the robustness of the photometry, performed in a consistent way among the different bands, and its multiwavelength nature: it is the most complete compilation of data for such a big sample of AGN in the EGS. This allows us to determine accurate photometric redshifts, and to distinguish clearly between the different groups of AGN. We have used a comprehensive set of AGN plus starburst templates from Polletta et al. (2007), to fit the SEDs of the galaxies in the sample, and to separate them in five different main groups. Through this classification, we can study the properties of the different types of AGN in this sample. Section 2 describes the sample and the cross-matching of the multiwavelength data, Section 3 explains the technique of classification of AGN based on the fit of their spectral energy distributions, in Section 4 the results of this paper are discussed, and finally in Section 5 the main conclusions are summarized. Throughout this paper we assume an  $H_0=75$  km s<sup>-1</sup> Mpc<sup>-1</sup> and a  $\Lambda$ CDM cosmology with  $\Omega_m=0.3$  and  $\Omega_\Lambda=0.7$ .

## 2. Sample and multi-wavelength data

The sample studied in this work, that comprises 116 AGN candidates, was built from the previously published X-ray catalogs found in Waskett et al. (2003), Nandra et al. (2005), and Barmby et al. (2006). These objects were originally selected by Barmby et al. (2006), both in the X-ray (Chandra and XMM-Newton) and in the mid-infrared (Spitzer). The X-ray and mid-infrared observations in the EGS are intermediate in depth and area between GOODS (Dickinson et al. 2001), the shallower NOAO Deep-Wide Field (Jannuzi & Dey 1999; Eisenhardt et al. 2004), and SWIRE (Lonsdale et al. 2003) surveys. Therefore, this region provides a valuable test of AGN properties at intermediate fluxes. In addition to this, we have compiled ultraviolet, optical, and near-infrared archival data for these AGN, in order

---

<sup>1</sup>The AEGIS project is a collaborative effort to obtain both deep imaging covering all major wavebands from X-ray to radio and optical spectroscopy over a large area of sky. <http://aegis.ucolick.org/index.html>

to increase the definition of their SEDs. These well-sampled SEDs allow us, first, to classify the objects in different galaxy population groups and calculate their photometric redshifts, and secondly, to study the physical properties of this representative sample of AGN.

The Chandra data were taken with ACIS-I in 2002 August (Nandra et al. 2005), consisting of a 200 ks exposure with a limiting full-band flux (0.5-10 keV) of  $3.5 \times 10^{-16}$  erg cm $^{-2}$  s $^{-1}$ . The XMM-Newton data were obtained in 2000 July with a 56 ks exposure and with a limiting 0.5-10 keV flux of  $2 \times 10^{-15}$  erg cm $^{-2}$  s $^{-1}$  (Waskett et al. 2003). Barmby et al. (2006) combined both catalogues producing a list of 152 sources within the limits of the Spitzer mid-infrared observations.

The Spitzer data (IRAC and MIPS) are part of the Infrared Array Camera Deep Survey, taken during 2003 December and 2004 June-July with 2.7 hr exposure per pointing. In the case of the MIPS data, the observations were done in 2004 January and June with a depth of 1200 s per pointing. The  $5\sigma$  limiting AB magnitudes are 24.0, 24.0, 21.9, and 22.0 for the IRAC bands, and 19.1 in the case of MIPS. Barmby et al. (2006) finally selected 138 objects with secure detections in all four IRAC bands, out of the 152 X-ray emitters. The detection of these objects in both the X-rays and the mid-infrared gives confidence in their classification as AGN. Besides, we have also checked that the values of the hard X-ray and 24  $\mu$ m fluxes lie inside the AGN-characteristic region (see Figure 1 of Alonso-Herrero et al. (2004)).

In addition to the previous, we have compiled near and far-ultraviolet images from the GALEX GR2/GR3 data release ( $3\sigma$  limiting AB magnitudes = 25 in both Far- and Near-UV filters); optical images from the CFHT Legacy Survey, T0003 worldwide release (Gwyn et al., in preparation), taken with the MegaCam imager on the 4 m Canada-France Hawaii Telescope (Boulade et al. 2003) ( $5\sigma$  limiting AB magnitudes = 26.3, 27.0, 26.5, 26.0, and 25.0 in u,g,r,i, and z bands); and J and  $K_S$  data from the version 3.3 of the Palomar-WIRC K-selected catalog of Bundy et al. (2006), ( $5\sigma$  limiting Vega magnitudes = 23 and 20.6 in the J and  $K_S$  bands).

The fluxes employed in this work have been measured in a compilation of publicly available imaging data, which is outlined briefly in Villar et al. (2008) and will be described in detail in Barro et al., in preparation (see also Pérez-González et al. (2008b)). Photometry in consistent apertures was measured in all bands with available imaging data following the procedure described in Pérez-González et al. (2005, 2008a). In the near-infrared, no deep J- and  $K_S$ -band imaging data were available and we have used the photometric catalogs published by Bundy et al. (2006). The same happens with the X-ray data, that have been drawn from the catalogs (Waskett et al. 2003; Nandra et al. 2005; Barmby et al. 2006).

We have performed the cross-matching of the 138 sources between the X-ray and Spitzer data, adding ultraviolet, optical, and near-infrared data points, avoiding the false matches that Barmby et al. (2006) expected in their sample. We identify these objects through their IRAC positions in our merged photometric catalog (Pérez-González et al. 2005, 2008a). The source coordinates on the IRAC 3.6  $\mu\text{m}$  images are then cross-correlated with each one of the ultraviolet, optical and near-infrared catalogs using a search radius of  $2.5''$ , starting with the deepest images. When a source is identified in one of these images, the Kron (1980) elliptical aperture from this reference image is taken and overlaid onto each of the other bands. The aperture employed is large enough to enclose the PSF in all the ultraviolet, optical and near-infrared images (the seeing being less than  $1.5''$ ). For IRAC and MIPS, because of their large PSFs, integrated magnitudes measured in small apertures (applying aperture corrections) are employed. The hard and soft X-ray fluxes are obtained by cross-correlating the IRAC positions with the X-ray catalogs, using a search radius of  $2''$  in this case. Uncertainties of each measured flux are obtained from the sky pixel-to-pixel variations, detector readout noise, Poisson noise in the measured fluxes, errors in the World Coordinate System, and errors in the absolute photometric calibration.

In some cases, for a single IRAC source, there are several counterparts in the ground-based images within the  $2.5''$  search radius. For these objects, the ground-based optical/near-infrared reference image is used to determine the positions of each source separately. The IRAC images are then deconvolved using the IRAC PSFs. Although the IRAC PSFs have FWHMs of approximately  $2''$ , determination of the central position of each IRAC source can be performed more accurately, and sources can be resolved for separations  $\sim 1''$  from each other. IRAC fluxes are then remeasured by fixing the positions of the objects in each pair, and by scaling the flux of each object in an aperture of  $0.9''$ . For a more detailed description of the cross-matching and aperture photometry see Pérez-González et al. (2005, 2008a).

Out of the 138 sources that comprise the final sample chosen by Barmby et al. (2006), we find 96 sources that have unique detections in all bands, plus other 20 objects with double detection in the ground-based images. We discard the remaining 22 objects because 21 of them show multiple (more than two) detections in the optical/near-infrared images, leading to possible source confusion, plus another object that shows a star-like SED. The analysis of the data will be done first for the 96 objects that are definitely free from contamination from other sources. Nevertheless, in Section 4.5, we analyse the images and photometric redshifts of those additional 20 objects with double detection.

### 3. Spectral energy distributions and photometric redshifts of objects with unique detection.

In order to classify the 96 spectral energy distributions and to estimate their photometric redshifts, we combine optical (u,g,r,i,z), near-infrared (J,K), and mid-infrared data (IRAC 3.6, 4.5, 5.8, 8  $\mu\text{m}$  and MIPS 24  $\mu\text{m}$ ) to build well-sampled SEDs that we then fit with the library of starburst, AGN and galaxy templates taken from Polletta et al. (2007). We make use of the photometric redshift code HyperZ (Bolzonella et al. 2000) to perform the fits. This code determines the best photometric redshifts ( $z_{\text{phot}}$ ) by minimization of the  $\chi^2$  derived from a comparison between the photometric SEDs and the set of template spectra, leaving the redshift as a variable. The code also takes into account the effects of dust extinction according to the selected reddening law (Calzetti et al. 2000). Choosing a wide range of reddening values seems to be essential to reproduce the SEDs of high redshift galaxies (Bolzonella et al. 2000). According to Steidel et al. (1999), the typical E(B-V) for galaxies up to  $z \sim 4$  is 0.15 mag, thus  $A_V \sim 0.6$  mag when using the Calzetti’s law. The maximum  $A_V$  allowed in our calculations is about 2 times this value, thus  $A_V$  ranges from 0.0 to 1.2, with a step between them of 0.3. Similar values of  $A_V$  are typically chosen in the literature (Bolzonella et al. 2000; Babbedge et al. 2004).

The chosen set of templates contains 23 SED-types, that we have arranged into the following five main groups: *Starburst-dominated AGN* (which includes four Starbursts and Starburst/ULIRGs templates), *Starburst-contaminated AGN* (three templates, namely: Starburst/ULIRG/Seyfert 1, Starburst/Seyfert 2, and Starburst/ULIRG/Seyfert 2), *Type-1 AGN* (three Type-1 QSO templates), *Type-2 AGN* (Type-2 QSO, Torus-QSO, Seyfert 1.8, and Seyfert 2 templates), and finally, *Normal galaxy hosting AGN* (nine templates including 2, 5, and 13 Gyr ellipticals plus S0, Sa, Sb, Sc, Sd, Sdm type spirals). These templates span the range in wavelength between 0.1 and 1000  $\mu\text{m}$ . For a detailed explanation of their synthesis see Polletta et al. (2007). Our main interest is to classify all of our sources into these five main groups and to determine the distribution of the sources into each of these groups. Notice that although all of the sources are AGN, the *Starburst-dominated AGN* have their SEDs dominated by the starburst emission from the optical to the mid-infrared; the *Normal galaxy hosting AGN* would be low-luminosity AGN embeded in an otherwise normal galaxy emission; and in the case of the *Starburst-contaminated AGN*, the emission of both the starburst or the AGN dominate depending on the wavelength we are looking at. Indeed, some of these objects show noticeably the AGN power-law beyond the near-infrared.

We fit data from the optical  $u$  band up to the MIPS 24  $\mu\text{m}$  band. We avoid the use of GALEX data because few galaxies have these, and because their use introduce big errors in the fits. As explained in Polletta et al. (2007), including mid-infrared data improves



considerably the photometric redshift calculations, since some spectral types suffer degeneration that is broken by the non-extinguished longer wavelengths, even if the errors in the magnitudes are larger in the mid-infrared than in the optical and near-infrared bands.

Examples of HyperZ fits for each of the employed templates are shown in Figure 1. In the *Type-2 AGN* panel, only three templates are shown because none of the 96 galaxies were fitted with the Torus-QSO template. The *Normal galaxy hosting AGN* panel contains only one example of elliptical template (the 2 Gyr elliptical) and one example of spiral (Sb). See Table 1 to check the SED types and their corresponding group. Photometric redshifts derived from the fits are reported in Table 1, together with the  $\chi^2_\nu$  and probabilities given by HyperZ, the  $A_V$ , and the template used for the fit of each galaxy. In the cases where spectroscopic redshifts are available, these are also given in Table 1.

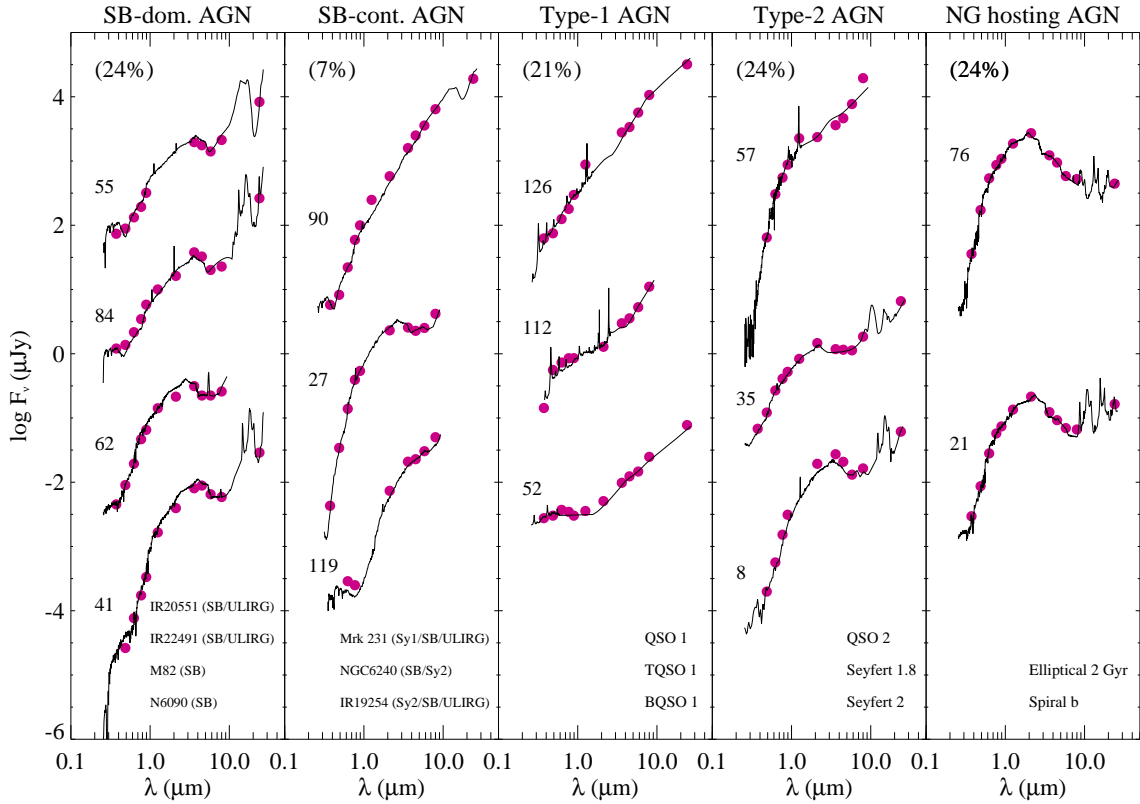


Fig. 1.— Examples of SEDs in our sample (dots) fitted with different templates from Polletta et al. (2007) for the five main groups considered. The legends in the bottom right of each panel refer to the actual template within the groups from Polletta et al. (2007). The data have been scaled for clarity. The X-axis corresponds to observed wavelength. The fifteen galaxies represented here are labelled with the ID from Table 1. The percentages of objects enclosed in each group are typed in the upper left corner of each panel.

A comparison between the photometric and spectroscopic redshifts for the 39 sources with publicly available  $z_{spec}$  from the DEEP data archive (Weiner et al. 2005) is shown in Figure 2. Notice that only 31 out of these 39 galaxies have reliable spectroscopic redshifts (flag = 3 or 4 in the DEEP data archive). Horizontal error bars indicating the reliability of the  $z_{spec}$  are represented in Figure 2, together with vertical error bars that indicate the discrepancies between the  $z_{spec}$  and  $z_{phot}$ . The dashed lines represent 20% agreement in  $(1+z)$ . The fractional error  $\Delta z = \frac{z_{phot} - z_{spec}}{1 + z_{spec}}$  quantifies the number of catastrophic outliers, which are those with  $|\Delta z| > 0.2$ . Our measured mean  $\Delta z$  for the 39 sources with spectroscopic redshifts is 0.05, with a  $\sigma_z = 0.37$ , and an outlier fraction of  $\sim 18\%$ , corresponding to seven discordant objects, labelled in Figure 2. However, if we consider only the 31 objects with reliable  $z_{spec}$  (flags = 3 or 4),  $\Delta z = -0.03$ , and  $\sigma_z = 0.11$ , with three outliers (8%). These results point to the goodness of our fits, and thus we rather trust our photometric redshifts better than the spectroscopic ones for the outliers indicated (all of them with  $z_{spec}$  with flags = 1 or 2 in the DEEP database). We nevertheless note a slight underestimation of our photometric redshifts (see Figure 2) in comparison with the spectroscopic ones ( $\Delta z = -0.03$ ). Although this effect is negligible, we are aware of it, and we assume that all the calculated  $z_{phot}$ 's might be affected by this slight underestimation.

Based on the good agreement between spectroscopic and photometric redshifts in this fairly large subsample of sources (the results shown are better than those typically obtained for AGN samples (Babbedge et al. 2004; Kitsionas et al. 2005; Bundy et al. 2008) and with practically the same  $\sigma_z$  and outlier fraction than those reported by Polletta et al. (2007)), we can confidently extrapolate the results to the rest of the sample. This, together with the SED classification into the five groups described above, allows us to perform a reliable statistical analysis of the different AGN populations.

It is worth to mention that the distribution of object type in the subsample with spectroscopic redshifts is completely different from the total sample. Considering only the 31 objects with highly reliable  $z_{spec}$ , there are 4 *Starburst-dominated AGN*, 4 *Starburst-contaminated AGN*, 3 *Type-1 AGN*, 5 *Type-2 AGN*, and 15 *Normal galaxy hosting AGN*. Thus, it is very difficult to check the redshift failure rate for the different groups. Only for the *Normal galaxy hosting AGN* we can confirm the success in the redshift determination with this set of templates, since  $\sim 50\%$  of the total number of objects fitted with elliptical or spiral templates have  $z_{spec}$  to compare with. Due to the flat and featureless SED typical of Type-1 QSOs, the *Type-1 AGN* group of templates could produce the less reliable photometric redshifts of the sample (Franceschini et al. 2005). We can not discard then that any subset of templates produces higher redshift failure rates than others, but looking at the distribution of the objects belonging to the different groups of AGN in the various diagnostic diagrams in the following sections, and at the correlations displayed by them, we are confident that our SED



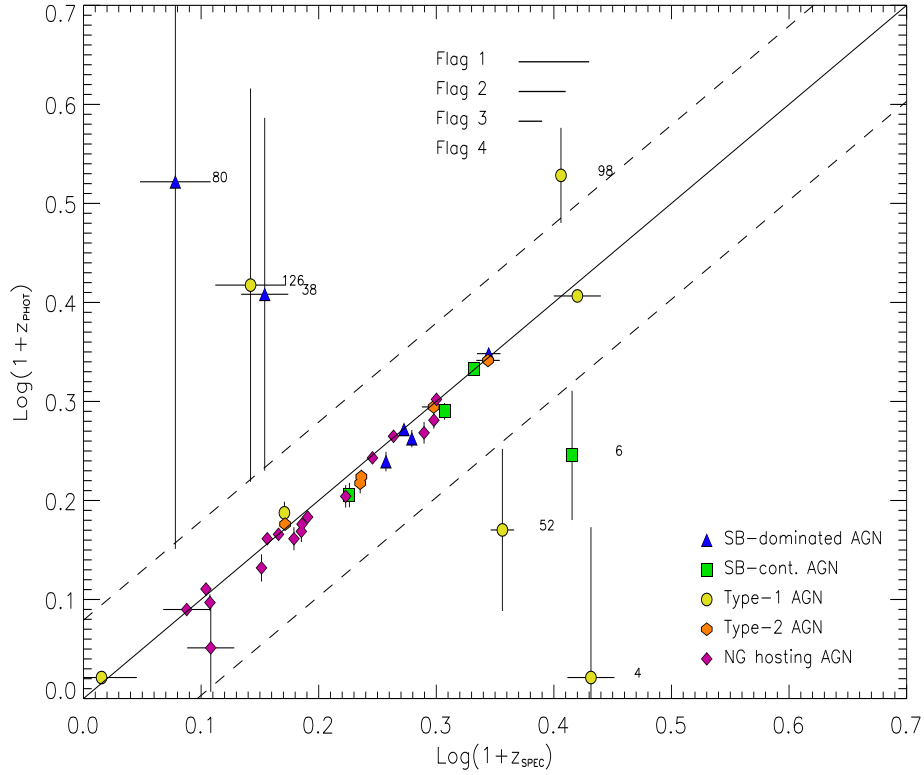


Fig. 2.— Comparison between photometric and spectroscopic redshifts for the 39 sources with publicly available  $z_{spec}$  from the DEEP data archive (Weiner et al. 2005). The solid line corresponds to  $z_{spec}=z_{phot}$ . Dashed lines represent 20% boundaries in  $(1+z)$ . Horizontal error bars indicating the reliability of the  $z_{spec}$  (flag=1 for the less reliable and flag=4 for the most reliable) are represented. Vertical error bars illustrate the discrepancies between the  $z_{spec}$  and  $z_{phot}$ . The seven outliers are labelled (4, 6, 38, 52, 80, 98 and 126). Note that there are only three outliers when only the 31 galaxies with reliable  $z_{spec}$  are considered.

classification and redshift determination are as good as for the *Normal galaxy hosting AGN* for the rest of the groups.

## 4. Discussion

### 4.1. Classification by SEDs and photometric redshift distribution of the sample.

Together with the photometric redshift calculations reported in the previous section, we obtain spectral energy distribution fits, that allow us to distinguish between different types

of AGN populations, i.e., whether they are pure AGN, AGN hosted by starburst-dominated galaxies, or AGN in otherwise normal galaxies.

For the five main groups described before we obtain the following distribution: *Starburst-dominated AGN* (24 % of the sample), *Starburst-contaminated AGN* (7 %), *Type-1 AGN* (21 %), *Type-2 AGN* (24 %), and *Normal galaxy hosting AGN* (24 %).

We consider the *Type-1 AGN*, *Type-2 AGN* and *Starburst-contaminated AGN* as representative groups of AGN-dominated galaxies (since their SEDs are AGN-like at all or almost all wavelength ranges). The *Starburst-dominated AGN* and *Normal galaxy hosting AGN* are likewise considered AGN somehow masked by their host emission. With this simple classification, we find that 52% of the sample is AGN-dominated while 48% is host galaxy-dominated; i.e., half of the objects in the EGS sample of AGN show AGN-like SEDs while the other half show host-dominated SEDs. This is consistent with the finding that between 40% and 60% of the Chandra-selected galaxies in the Hawaii Deep Survey Field SSA13 and in the Chandra Deep Field North (Barger et al. (2001) and Hornschemeier et al. (2001), respectively) have optical spectra with no-signs of nuclear activity.

Also Barmby et al. (2006), based on the IRAC slopes ( $\alpha < 0$  for the red power-law IRAC SEDs, and  $\alpha > 0$  for the blue ones) divided their sample in sources where the central engine dominates the IRAC SEDs and stellar-dominated galaxies. They found that 40% of the sources have red power-law SEDs, another 40% have blue host-dominated mid-infrared SEDs, and the remaining 20% could not be fitted with a power-law.

The method employed in this paper constitutes a powerful technique of classification of high redshift AGN provided we are able to procure well-sampled SEDs. This is important, for instance, for multi-band deep surveys of galaxies for which spectroscopic data will be necessarily scarce. Having SEDs over the largest wavelength range as possible is mandatory to identify the entire AGN population (Dye 2008). Otherwise, depending on the observed wavelength, the galaxies could be missclassified. This is crucial, for example, for our *Starburst-contaminated AGN*, that in the optical range look like starburst galaxies, and towards redder wavelengths appear as Type-1 or Type-2 AGN. Dye (2008) finds also that the results of the SED fitting show little difference between two filtersets that span the same wavelength range, despite the number of filters used. Nevertheless, from our work, we find that including a large number of filters can reveal details in the SED shape that help the code choosing between different templates. This is crucial to distinguish among the different templates of a given group, for which little differences in the SED determine the type of object, or its age (Polletta et al. 2007).

We use now the classification of the galaxies obtained to investigate the properties of

the different AGN groups. The distribution of redshifts for all the 96 objects with unique detection in our sample is shown in the top-left panel of Figure 3. 58% of the sample have  $z < 1$ , with the rest of the sources distributed in a decreasing tail up to  $z = 3$ . This is expected for X-ray selected samples with similar or even deeper flux limits (Hasinger 2003a; Barger et al. 2005). Figure 3 also shows histograms for the photometric redshift distributions of the *Starburst-dominated AGN*, *Starburst-contaminated AGN*, *Type-1 AGN*, *Type-2 AGN*, and the *Normal galaxy hosting AGN* groups.

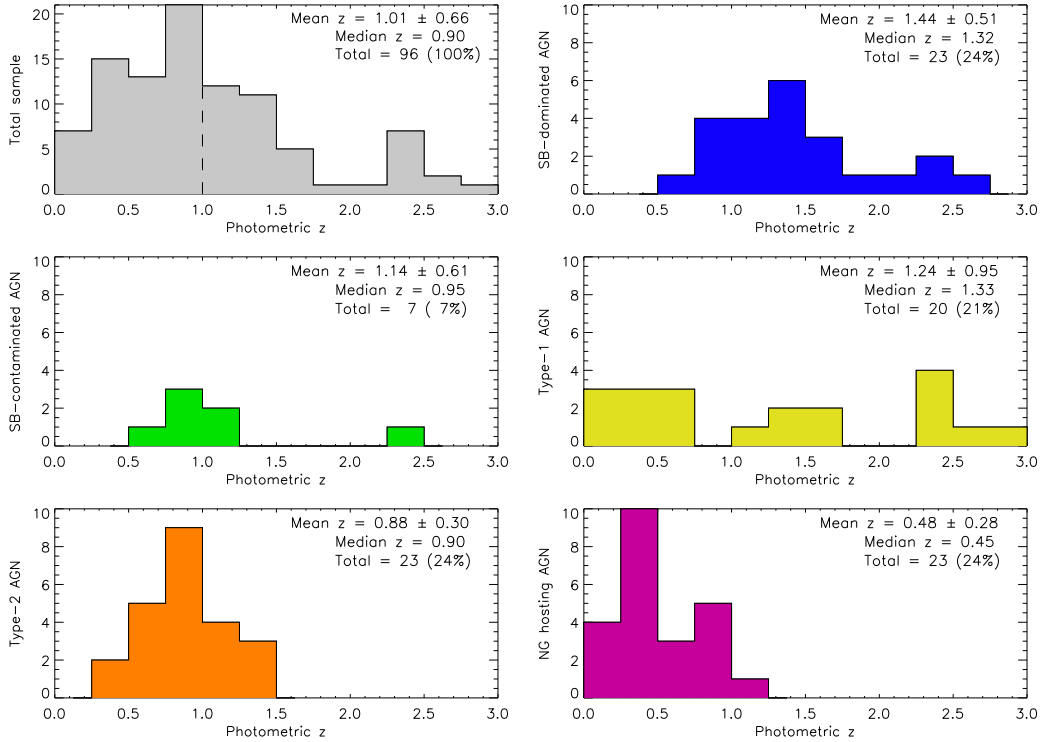


Fig. 3.— Distribution of photometric redshifts for the 96 objects with unique detection in our sample and for all the five main groups considered in this work. Mean photometric redshift for each group and corresponding standard deviation, together with the median redshift and the number of objects are labelled in each panel.

*Type-2 AGN* and *Normal galaxy hosting AGN* are concentrated at lower redshifts, whereas the *Starburst-dominated AGN* show a high concentration around  $z_{phot} = 1.3$ . The *Type-1 AGN* group has the largest spread in redshift, its mean value being  $z_{phot} = 1.24 \pm 0.95$ . The *Starburst-contaminated AGN* group contains only seven objects, six of them within the redshift range  $[0.6, 1.2]$ , the other having a  $z_{phot} = 2.45$ .

This indicates that the *Starburst-dominated AGN* constitute the high-redshift population of AGN masked by powerful host emission, whilst the *Normal galaxy hosting AGN*

group represents the low-redshift population of low-luminosity AGN also masked by their host galaxies. Previous studies suggest that most low luminosity AGN are found in massive, mostly spheroidal galaxies (Dunlop et al. 2003; Kauffmann et al. 2003; Grogin et al. 2005; Pierce et al. 2007). Something similar happens with the AGN-dominated group: the *Type-1 AGN* span a large redshift distribution, the *Starburst-contaminated AGN* are located at intermediate values of redshift, and finally, the *Type-2 AGN* are the low- $z$  objects in this subsample.

Alonso-Herrero et al. (2004) found that  $\sim 25\%$  of their X-ray and  $24\ \mu\text{m}$  selected sources in both the EGS and the Lockman Hole (45 in total) show pure type-1 AGN SEDs, while more than half of the sample have stellar emission-dominated or obscured SEDs. Franceschini et al. (2005) detected 99 AGN in the X-rays and mid-infrared with Spitzer in the SWIRE survey (Lonsdale et al. 2003), sorting them in three main groups: Type-1 AGN (39%), Type-2 AGN (23%), and normal and starburst galaxies (38%). By adding Piccinotti et al. (1982) and Kuraszkiewicz et al. (2003) samples, there are 32 AGN with  $z \leq 0.12$ , also selected both in the hard X-rays and mid-infrared, with more than half of these sources being type-1 AGN according to their SEDs. Ours and other works (e.g., Alonso-Herrero et al. (2004); Franceschini et al. (2005)) performed with SED classification of X-ray and mid-infrared selected AGN in a wide range of redshift (up to  $z \sim 2-3$ ), when compared with the results obtained for local samples of AGN selected in the same bands, seem to indicate that the percentage of type-1 objects decreases with redshift, while the number of obscured AGN at high redshift increases.

Although the data used in this paper do not allow a deep study of the AGN feedback phenomenon, it is worth noticing that a redshift sequence can be readily seen in Figure 3. Indeed, the *Starburst-dominated AGN* would have the highest redshifts in a decreasing sequence that goes through the *Type-1 AGN*, *Starburst-contaminated AGN*, and *Type-2 AGN*, ending with the *Normal galaxy hosting AGN* group, that shows the lowest redshifts. This evolutionary sequence has been noticed for early-type galaxies by Schawinski et al. (2007). According to this recent work, the starbursts would start and be the dominant player after its onset. Subsequently, as the BH accretes enough mass, the AGN feedback reveals itself as the BH competes for the gas reservoir with the starbursts eventually quenching the star formation. The starburst phase thus declines, the AGN becoming dominant. The *Starburst-contaminated AGN* phase would be the transition phase mentioned by Schawinski et al. (2007). This process continue through lower ionization phases and it will end with the more quiescent *Normal galaxy hosting AGN* phases at lower redshifts.

## 4.2. Correlations

### 4.2.1. Correlations for the whole sample

One of the main advantages of the sample we are discussing is the multiwavelength coverage of the data, which allows us to study for the first time various correlations between ultraviolet/optical/infrared luminosities and X-ray luminosities for such a big AGN sample and within this range of redshift. The aim is to understand the behaviour of these sources in the different wavelength ranges.

Absolute magnitudes ( $M_{ABS}$ ) computed by HyperZ in each filter using the photometric redshifts and the chosen cosmological parameters, are used here to derive luminosities for the 96 objects with unique detection. The HyperZ code provides the  $M_{ABS}$  (including the K correction) in the ultraviolet, optical, near- and mid-infrared filters considered. Regarding the X-ray data, the observed rest-frame hard and soft X-ray luminosities are obtained from the equation  $L_X = \frac{4\pi d_L^2 f_X}{(z+1)^{2-\Gamma}}$ , where  $d_L$  is the luminosity distance (cm),  $f_X$  is the X-ray flux (ergs  $\text{cm}^{-2} \text{s}^{-1}$ ), and  $\Gamma$  is the photon index. In this case, the K correction vanishes since we assume a photon index  $\Gamma = 2$  (Krumpe et al. 2007; Alexander et al. 2003; Mainieri et al. 2002), which is the canonical value for unobscured AGN (George et al. 2000). Obscured active nuclei have considerably flatter effective X-ray spectral slopes, due to the energy-dependent photoelectric absorption of the X-ray emission (Risaliti, Maiolino & Salvati 1999). However, Mainieri et al. (2002) find the same intrinsic slope of the X-ray spectrum for both type-1 and type-2 AGN whatever their absorption levels, with  $\Gamma \sim 2$  for an X-ray selected sample in the Lockman Hole. We therefore assume a photon index  $\Gamma = 2$  for either obscured and unobscured AGN, and consequently no K correction is needed for the X-ray luminosities.

The first row of Table 2 shows the fitting slopes and correlation coefficients ( $r$ ) of each scatter diagram between the far-UV/near-UV/ugriz/JK/IRAC/MIPS luminosities and the hard/soft X-ray luminosities for the fits including all the objects with unique detection. In all cases the Spearman’s rank correlation test has been performed, confirming that all the correlations are significant ( $p < 0.01$ ). Examples of these correlations for the far-UV/near-UV/r/K/IRAC  $4.5 \mu\text{m}$  /MIPS  $24 \mu\text{m}$  luminosities and the hard/soft X-ray luminosities are shown in Figure 4.

The expected slopes for AGN-dominated objects should be close to unity, since if the active nucleus is the dominant emitting source at all wavelengths, tight linear correlations should be drawn. Reality is different, and AGN are actually hosted by different types of galaxies. As it has been seen in previous sections, these host galaxies contaminate or even mask the AGN emission, thus deviating correlations from linear and worsening them. Both the X-ray and mid-infrared emissions are mostly dominated by the active nuclei, whereas

the optical and, to a lesser extent, the near-infrared bands are more affected by extinction, by stellar emission from the host galaxy, or by both. This is clearly reflected in the slopes and correlation coefficients (hereafter  $\alpha$  and  $r$ ) of the global fits (see first row of Table 2). Although correlations are all significant, with both the slopes and correlation coefficients close to unity, they begin getting slightly blurred as wavelength increases from the bluest optical bands up to the K band, improving again in the mid-infrared. The blurring is more noticeable when soft instead of hard X-rays are considered, due to the higher obscuration that affects the lower energies.

Correlations between ultraviolet and X-ray luminosities are also good. The slopes are  $\alpha \sim 1.2$  and  $1.1$  for the far-UV versus both the hard and soft X-rays luminosities, respectively, in good agreement with early X-ray studies of AGN that find correlations between X-ray and ultraviolet monochromatic luminosities with similar slopes:  $L_X \propto L_{UV}^\beta$ , with  $\beta \sim 0.7 - 0.8$ , thus  $\alpha \sim 1.4-1.2$  (Wilkes et al. 1994; Vignali et al. 2003; Strateva et al. 2005; Steffen et al. 2006). Nevertheless, this range of  $\alpha$  was determined by using 2 keV and 2500 Å luminosities, which correspond to soft X-rays and Near-UV, respectively. The slopes measured by us for the near-UV versus both the hard and soft X-rays luminosities are  $\alpha \sim 0.8$  and  $0.7$ , that are lower than expected. Nevertheless, LaFranca et al. (1995) found a correlation consistent with  $\alpha = 1$  using a generalized orthogonal regression that is in better agreement with our values.

#### 4.2.2. Correlations for the main AGN groups

We also report slopes and correlation coefficients for the five main groups considered in the last sections separately in Table 2. Spearman’s rank correlation tests have been performed for all scatter diagrams. Thus, the values reported in Table 2 correspond only to objects showing significant correlations ( $p < 0.01$ ).

Looking at the *Type-1 AGN* in Table 2 we conclude that they are the less contaminated active nuclei of the sample. Since we are seeing a direct view of the central engine, the emission is dominated by the AGN at all wavelengths. Therefore, these objects draw the most tight correlations between each photometric band and either the hard or the soft X-ray luminosities<sup>2</sup>.

---

<sup>2</sup>Note that in order to check that the good correlation displayed by *Type-1 AGN* luminosities is not due to a distance effect (this group of galaxies presents the largest spread in redshift, as shown in Figure 3), we have also analysed the corresponding fluxes, instead of luminosities, for all the groups considered in this section. This way, the distance effect is eliminated from the fits. We find the same linear and significant



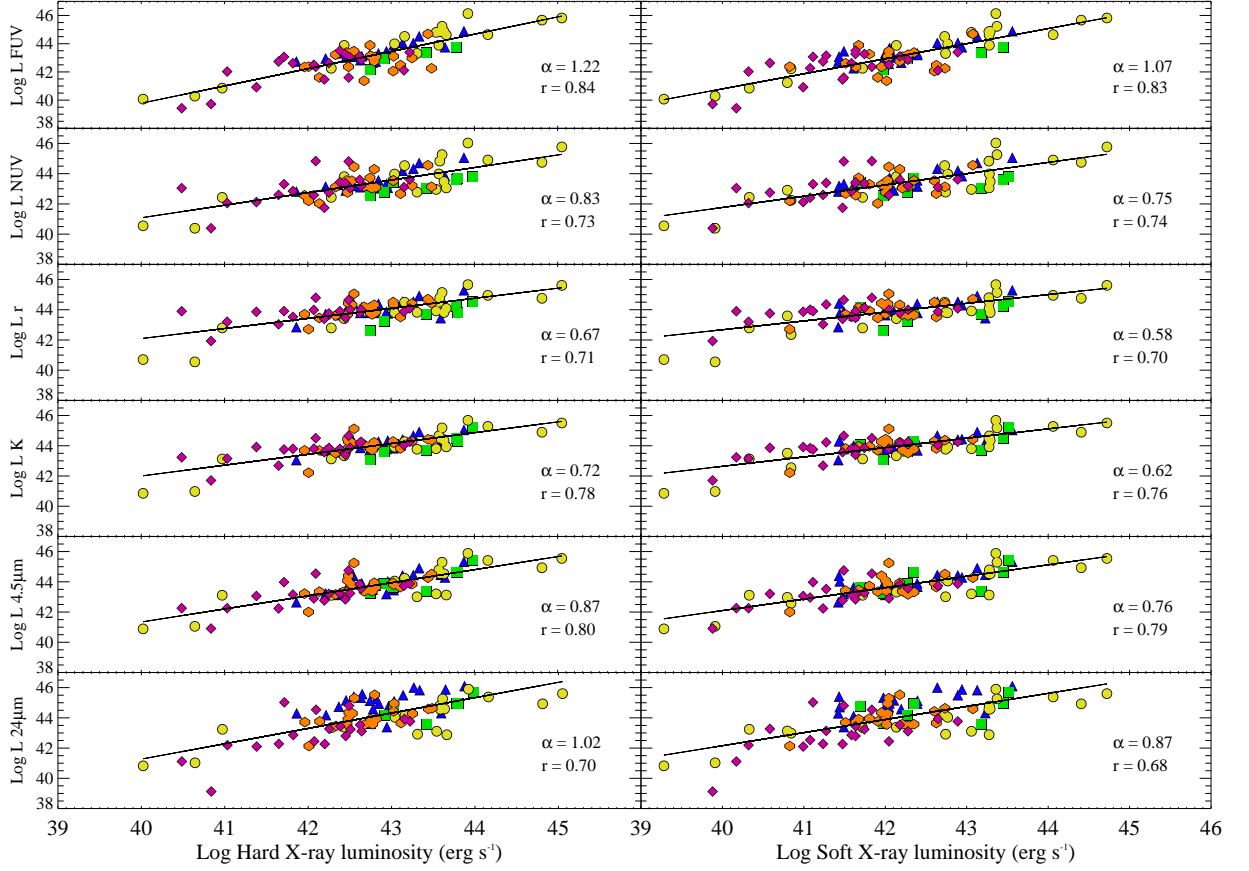


Fig. 4.— Examples of luminosity-luminosity scatter diagrams for all the objects in our sample with unique detections and published data in the considered bands. Logarithms of  $\nu L_\nu$  in the Far-UV, near-UV, r, K, IRAC 4.5  $\mu\text{m}$ , and MIPS 24  $\mu\text{m}$  bands ( $\text{erg s}^{-1}$ ) are represented versus their hard and soft X-ray counterparts. Symbols are the same as in Figure 2, indicating the template fitting classification.

If we look at the *Starburst-contaminated AGN*, we find significant correlations between the hard X-rays and the ultraviolet and infrared bands, disappearing for the soft X-rays, due to the higher obscuration in this wavelength range.

For the *Starburst-dominated AGN*, correlations including the hard X-ray data are better and more robust than those with the soft X-ray ones, for which both the slope and  $r$  values are far from unity. This is certainly due to the higher obscuration affecting the soft X-ray emission in these objects. The host galaxy emission and the dust are indeed masking the

---

correlations for *Type-1 AGN* fluxes, confirming that the correlations displayed for this group of AGN are only due to their intrinsic properties.

AGN. The same, but more dramatically, happens with the *Type-2 AGN* group, for which all the correlations involving the soft X-ray emission are not significant.

It is worth to mention the worsening of the fits for the *Starburst-dominated AGN* when the hard X-ray and either the IRAC 8  $\mu\text{m}$  or MIPS 24  $\mu\text{m}$  emission are considered. The slopes and correlation coefficients of both fits move away from unity, something that is interpreted as due to the increasing importance of the starburst emission at these longer wavelengths. If we look at the MIPS 24  $\mu\text{m}$  luminosity-luminosity scatter diagrams (bottom of Figure 4), the overall majority of the *Starburst-dominated AGN* are located above the fit line. This indicates that there is an excess of mid-infrared emission, as compared with the X-ray luminosity coming principally from the AGN. This mid-infrared excess comes from warm dust heated by the intense star formation bursts taking place in the galaxy (in addition to the dust heated by the AGN), hence deviating the *Starburst-dominated AGN* group from the linear fit, and making the correlation non-significant when the MIPS 24  $\mu\text{m}$  luminosity is considered.

The behaviour of *Normal galaxy hosting AGN* is completely different: correlations when either the soft or hard X-rays are considered are quite similar, improving towards longer wavelengths, where the AGN resurfaces. This group of galaxies include low-luminosity AGN hosted in normal galaxies that dominates the optical and near-infrared bands, but not the mid-infrared emission. This explain why in some fits performed with this subset of templates, the IRAC 8 and MIPS 24  $\mu\text{m}$  are not completely well reproduced by the fit.

### 4.3. X-ray properties

Looking at the hard and soft luminosity ranges (see Table 3) for each of the five main groups described above, we find that *Type-1 AGN* present the largest spread in luminosity, together with the highest luminosity values in both bands ( $L_{\text{Hard}} = 10^{40-45}$  and  $L_{\text{Soft}} = 10^{39-45} \text{ erg s}^{-1}$ , not corrected for absorption). Alonso-Herrero et al. (2006) found that the majority of galaxies in their sample of X-ray detected sources in the CDF-S fitted with Broad-line AGN (BLAGN) QSO templates showed hard X-ray luminosities in the range  $10^{43-44} \text{ erg s}^{-1}$  (also not corrected for absorption). The same has been found when a spectroscopic classification of the objects has been possible (Zheng et al. 2004; Szokoly et al. 2004; Barger et al. 2005). Our hard X-ray luminosity range for *Type-1 AGN* agrees with the literature in the sense that the most luminous X-ray sources are enclosed in that range, whilst five sources show  $L_{\text{Hard}} < 10^{43} \text{ erg s}^{-1}$ , and only three have  $L_{\text{Hard}} < 10^{42} \text{ erg s}^{-1}$ , namely irac068644, irac027980, and irac018192, all of them with  $z_{\text{phot}} < 0.2$ . The most X-ray luminous AGN in our sample is irac040934, with a  $L_{\text{Hard}} = 10^{45} \text{ erg s}^{-1}$  and  $z_{\text{phot}} = 2.42$ .

The behaviour of the *Starburst-contaminated AGN* is very similar to that of the majority of the *Type-1 AGN* and exactly coincides with the hard X-ray luminosity range found by Alonso-Herrero et al. (2006) for BLAGN-fitted objects. This indicates that, despite the starburst appearance of the SEDs of these objects at longer wavelengths, in regard to their X-ray emission their AGN nature dominates.

The *Starburst-dominated AGN* are contained in a narrower interval of X-ray luminosities ( $L_{Hard} = 10^{42-44} \text{ erg s}^{-1}$  and  $L_{Soft} = 10^{41-44} \text{ erg s}^{-1}$ ), although reaching high values, indicating that these galaxies are not only starbursts, but also masked-AGN that show strong emission in their X-ray emission. Indeed, very few *bona fide* starburst galaxies have  $L_X > 10^{42} \text{ erg s}^{-1}$ , even including luminous sources at moderate redshifts (Zezas, Alonso-Herrero & Ward 2001). Only for warm ultraluminous infrared galaxies (ULIRGs) luminosities of up to  $10^{42} \text{ erg s}^{-1}$  are expected (Franceschini et al. 2003). *Type-2 AGN* display hard X-ray luminosities ranging from  $10^{42}$  to  $10^{43} \text{ erg s}^{-1}$ , staying in a much narrower range and with lower values than those of *Type-1 AGN*. The values of hard X-ray luminosities that we find for *Starburst-dominated AGN* and *Type-2 AGN* coincide with those found by Alonso-Herrero et al. (2006) for their galaxies fitted with Narrow-line AGN (NLAGN)+ULIRG templates.

Finally, the *Normal galaxy hosting AGN* group shows the lowest luminosity range of any of the groups ( $L_{Hard} = L_{Soft} = 10^{40-43} \text{ erg s}^{-1}$ ), which is consistent with the fact that they are hosting low-luminosity AGN (Dunlop et al. 2003; Kauffmann et al. 2003; Grogin et al. 2005; Pierce et al. 2007). The hard X-ray luminosity range of this group of objects coincides with typical luminosities ( $L_{Hard} < 2 \times 10^{42} \text{ erg s}^{-1}$ ) of the local cool ULIRGs population, except for four sources, namely irac045337, irac019616, irac016716, and irac049420.

These results, together with the mean redshift of each group reported in Section 4.1., point out that the evolution of AGN is luminosity-dependent, with low-luminosity AGN peaking at lower redshifts than luminous active nuclei (Hasinger 2003a; Hasinger et al. 2005; Fiore et al. 2003; Ueda et al. 2003; LaFranca et al. 2005; Brandt & Hasinger 2005; Bongiorno et al. 2007).

#### 4.4. Infrared and optical properties

The IRAC mid-infrared colors have been used as a diagnostic tool to separate AGN from non-active galaxies and stars in different samples (Lacy et al. 2004; Hatziminaoglou et al. 2005; Stern et al. 2005; Alonso-Herrero et al. 2006; Barmby et al. 2006; Donley et al. 2007). Particularly, Stern et al. (2005) show an IRAC color-color diagram for the AGES sample, with all their objects spectroscopically classified. They found that BLAGN are clearly sepa-

rated from Galactic stars and ordinary galaxies in their diagram, with the NLAGN located both inside and outside of the active galaxies area.

An IRAC colour-colour diagram for our sample is represented in Figure 5. The different symbols indicate the template fitting classification. The dashed line in Figure 5 corresponds to the Stern et al. (2005) empirical separation of AGN in their sample. In our case, this region includes all the *Type-1 AGN*, and all but one of the *Starburst-contaminated AGN*. This is expected, since five of the seven galaxies belonging to that group were fitted with the Sy1/SB/ULIRG template (SED type = 4, see Table 1), while the one located outside the AGN region was fitted with the Sy2/SB template (SED type = 6).

The only-galaxy classified as *Starburst-contaminated AGN* fitted with a Sy2/SB/ULIRG template (SED type = 13) that is contained in the Stern et al. (2005) AGN region is irac046309, its photometric redshift being  $z=2.45$ . The redshift of this source is mentioned here because, as Barmby et al. (2006) discuss and illustrate in their Figure 6, the AGN-dominated templates have red mid-infrared colors and thus, lie inside the Stern et al. (2005) region at all redshifts, whereas the star-forming galaxy templates begin to move into this area as the redshift increases. This explains why all *Type-1 AGN* are located inside the AGN region marked by the dashed line, as well as the six *Starburst-contaminated AGN*: five are fitted with the Sy1/SB/ULIRG template, and the galaxy irac046309 is a high redshift Sy2/SB/ULIRG. The *Normal galaxy hosting AGN*-fitted objects (that have the bluest IRAC colors of the sample) are excluded of this region (except for one of them).

As shown in Stern et al. (2005), the active galaxy region is contaminated with Galactic stars and normal galaxies, with the NLAGN located both inside and outside of this area. The same happens in our Figure 5: *Starburst-dominated AGN* and *Type-2 AGN* are partly contained in this area, and partly not. We have estimated the mean redshifts of both groups of galaxies for the in- and out-objects, finding that the *Starburst-dominated AGN* lying outside the pure-AGN region have a mean  $z = 1.35 \pm 0.54$ , while those inside have a mean  $z = 1.52 \pm 0.50$ . Following the same trend, the Type-2 AGN mean redshift is  $z = 0.79 \pm 0.26$  for the outside objects, and  $z = 0.97 \pm 0.32$  for the galaxies included in the Stern et al. (2005) region. This is again consistent with the evolution of mid-infrared colors with redshift for star-forming galaxies (Barmby et al. 2006; Donley et al. 2008). However, these mean redshifts for *Starburst-dominated AGN* and Type-2 AGN lying inside and outside the Stern et al. (2005) region are only orientative, since the differences between them are not statistically significant.

The reliability of these type of diagram (mid-infrared color selection) in selectioning AGN have been questioned in the literature (Cardamone et al. 2008; Donley et al. 2008). It seems that they fail to identify a large number of X-ray selected AGN, finding only the most

luminous. In our work, the Stern et al. (2005) region wraps all the Type-1 objects, all but one of the *Starburst-contaminated AGN*, and half of the *Starburst-dominated AGN* and Type-2 AGN. 52% of our sample is included in this area, but the low-luminosity AGN (most of them *Normal galaxy hosting AGN* and several *Starburst-dominated AGN* and *Type-2 AGN*) are excluded. Cardamone et al. (2008) find that 76% of their spectroscopically-selected BLAGNs fall inside this region, but only 40% of the X-ray selected objects are included. Summarizing, although the diagram in Figure 5 only includes half of our sample in the Stern et al. (2005) region, it seems very effective segregating the different AGN groups.

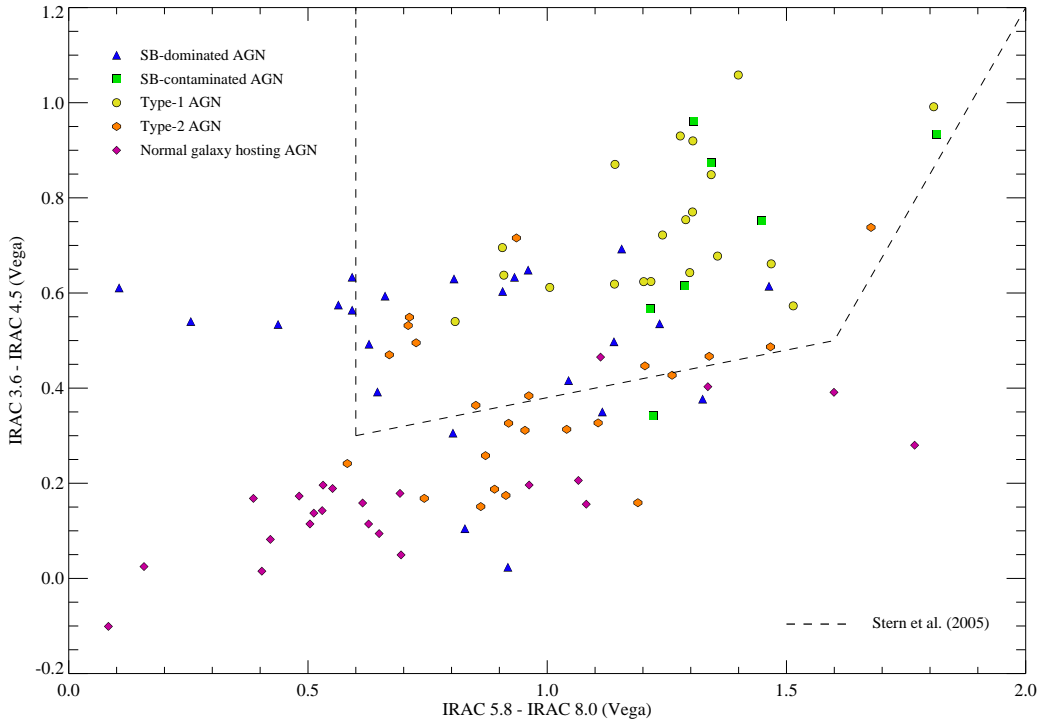


Fig. 5.— IRAC color-color plot for the 96 sources in our sample. Symbols are the same as in Figure 2, indicating the template fitting classification. The dashed line corresponds to the Stern et al. (2005) empirical separation of AGN in their sample.

The left pannel of Figure 6 shows the mid-infrared  $24\ \mu\text{m}$  to optical ( $r$  band) flux ratio versus the  $(r-z)_{AB}$  color for galaxies with unique detection. The  $24\ \mu\text{m}$  to optical flux ratio is a rough estimator of obscured activity in galaxies, since the  $24\ \mu\text{m}$  sources with faint optical counterparts should be luminous AGN obscured by dust and/or gas in the optical range (Fiore et al. 2008). The  $(r-z)_{AB}$  color depends on the obscuration present in the galaxy.

As expected for pure AGN, we find a significant correlation between the  $24\ \mu\text{m}$  to  $r$  flux ratio and  $(r-z)_{AB}$  for the *Type-1 AGN* and *Type-2 AGN*, because the nuclear emission

dominates both in the optical and mid-infrared wavelengths (Fiore et al. 2008). However, the correlation is not significant for the *Starburst-dominated AGN* group, since they have an excess in their mid-infrared emission, coming from the dust heated by the starbursts, in addition to the dust heated by the AGN. *Normal galaxy hosting AGN* display also a correlation between the two quantities, but with a different slope and lower correlation coefficient than the pure AGN objects. The corresponding slopes and correlation coefficients are indicated in Figure 6, except for the *Starburst-contaminated AGN* group, due to the low number of objects fitted with this set of templates.

A segregation between the different groups is noticeable in the plot: the *Starburst-dominated AGN* and *Starburst-contaminated AGN* are shifted towards the highest values of the mid-infrared to optical ratio  $\text{Log} (24 \mu\text{m} / \text{r band flux}) > 1.6$ , *Type-1 AGN* and *Type-2 AGN* are located at intermediate values, and the *Normal galaxy hosting AGN* have the lowest values of this ratio ( $\text{Log} [24 \mu\text{m} / \text{r band flux}] < 1.8$ ). Obscured AGN should be located towards the top right of Figure 6 (left pannel), since they have the reddest optical colors and the highest  $24 \mu\text{m}/\text{r}$  band flux ratios. *Starburst-dominated AGN*, *Starburst-contaminated AGN*, and *Type-2 AGN*-fitted objects are the most obscured galaxies in our sample, according to this diagram, although they are not as obscured as those in Fiore et al. (2008). We have chosen the  $(\text{r-z})_{AB}$  color instead of the most common  $(\text{r-K})_{AB}$  due to the lower number of objects that have available K magnitudes.

In the right pannel of Figure 6 the same mid-infrared  $24 \mu\text{m} / \text{r}$  band flux ratio is shown against the  $(\text{r-IRAC } 3.6 \mu\text{m})_{AB}$  color for galaxies with unique detection. As much as the  $(\text{r-z})_{AB}$  color is contaminated by the host galaxy contribution, the  $(\text{r-IRAC } 3.6 \mu\text{m})_{AB}$  color is dominated by the hot dust emission heated by the AGN and/or intense star formation (Brusa et al. 2005). In this case, all the individual groups of objects as well as the whole sample show significant and tight correlations. The segregation between the different groups mentioned before is clear again in this graph. The *Starburst-dominated AGN* and *Starburst-contaminated AGN* clearly show the reddest colors of the sample ( $\text{r-IRAC } 3.6 \mu\text{m} > 2.3$ ), while the *Normal galaxy hosting AGN* display the bluest, concentrated around  $\text{r-IRAC } 3.6 \mu\text{m} \sim 1.6$ . These objects occupy the left bottom corner of the right pannel of Figure 6 because the host galaxy outshines the AGN emission at all wavelengths (except in the X-rays).

#### 4.5. Objects with double detection in the optical bands.

Twenty out of the 116 objects that comprise our full sample show double detection in the ground-based images, thanks to their better spatial resolution. Figs. 7 and 8 show ACS V-band/HST images of both detections (indicated with circles) for each pair of galaxies,



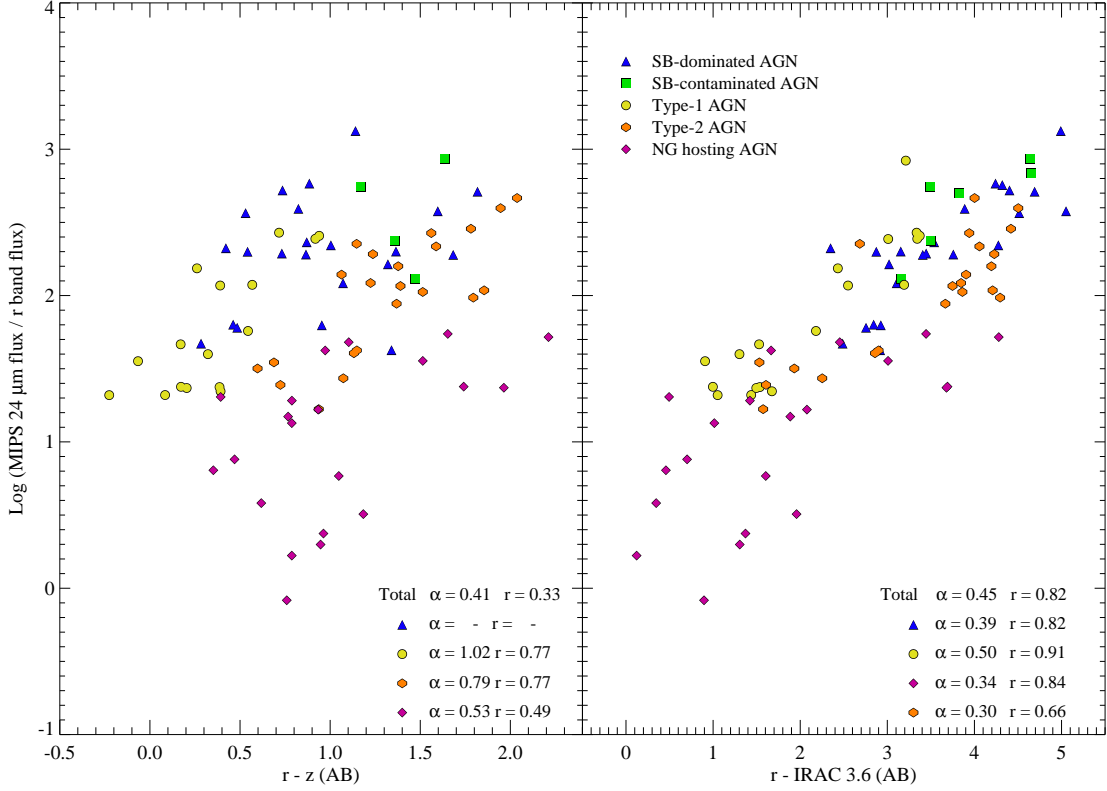


Fig. 6.— Log (MIPS 24  $\mu$ m / r band) flux ratio versus the r-z (AB) color for objects with unique detection in our sample and available r and z magnitudes (left panel) and the same ratio versus the r-IRAC 3.6  $\mu$ m color (right panel). The slopes and correlation coefficients are labeled for the global fit and for each of the four groups.

except for objects irac053271 and irac038708, which do not have HST imaging, and for which optical CFHTLS r-band images are shown instead. The CFHTLS magnitudes have been employed for the calculations with the HyperZ code, although we have chosen the HST images for display purposes, because of their better resolution. These images help us classifying morphologically these 20 objects with double detections as either interacting systems, different star forming regions of the same galaxy, or simple source confusion, as described in Table 4.

In the case of these objects with double detection, for a single IRAC source, there are two counterparts in the ground-based images within the 2.5'' search radius. As described in Section 2, the optical/near-infrared reference image is used to determine the positions of each source. The IRAC images are then deconvolved using the IRAC PSFs. The sources can be resolved for separations  $\sim 1''$  from each other, and IRAC fluxes are then remeasured by

fixing the positions of the objects in each pair, and by scaling the flux of each object in an aperture of  $0.9''$  (Pérez-González et al. 2005, 2008a). The integrated magnitude is derived applying an aperture correction based on empirical IRAC PSFs (for the  $0.9''$  aperture the factors are  $1.01 \pm 0.07$ ,  $1.02 \pm 0.08$ ,  $1.2 \pm 0.10$ , and  $1.44 \pm 0.14$  for the channels 3.6, 4.5, 5.8, and  $8.0 \mu\text{m}$ , respectively). See Pérez-González et al. (2008a) appendix for more details. The flux contamination is found to be smaller than the 10% in most cases, an even smaller for the non-infrared-bright sources.

Once we know the positions of each galaxy in a pair, we can check whether the mid-infrared emission comes from both, or just from one of the objects in the IRAC and MIPS images. In the majority of the cases, all the mid-infrared flux in a pair of galaxies comes from only one of the objects (see Table 4), the other probably being a non-active object. Then, we assume that the X-ray emission comes from the same mid-infrared emitter, and we calculate photometric redshifts for the active objects only.

In those cases where the mid-infrared emission can not be allocated clearly to one of the objects (irac038708, irac056633, and irac046783), photometric redshifts calculated by HyperZ for both sources in each pair have been obtained and they are reported in Table 5 together with their  $\chi^2_\nu$ , probabilities, SED type and  $A_V$ . For the other 17 pairs of galaxies, for which the mid-infrared emission comes clearly from only one of the objects, we calculate photometric redshifts only for the mid-infrared emitter. Spectroscopic redshifts from the DEEP database are also given, when available, together with their corresponding reliability flags. Unfortunately, this is the case for only four objects, and all of them with low reliability flags (1 or 2, see Table 5). Nevertheless, we can assume that the photometric redshifts, obtained as described in Section 3, are reasonably good, since we have followed the same methodology as for the 96 sources with single detections.

As reported in Table 4, irac056633\_2, irac036704\_1, irac022060\_1, irac029343\_1, and irac019604\_1 are interacting systems themselves, as can be seen in the HST images (Figs. 7 and 8). These sources must be treated with caution, since their fluxes could be contaminated with extra-emission coming from their companions. This fact explains the low probabilities of the HyperZ fits for objects irac056633\_2, irac029343\_1, and irac019604\_1, reported in Table 5.

In the same way as we have done for the objects with unique detection in previous sections, we distribute here the 23 template fitted-objects with double detection in the same five main categories described before. The percentages for each group are: *Starburst-dominated AGN* (48 % of the mid-infrared emitters), *Starburst-contaminated AGN* (0 %), *Type-1 AGN* (17 %), *Type-2 AGN* (22 %), and *Normal galaxy hosting AGN* (13 %). Note that for this subsample of objects with double detection, almost half of the objects are

described by starburst-type SEDs. If, as in Section 4.1., we split the objects into AGN-dominated and host-dominated galaxies, we find that 39% show AGN-like SEDs while 61% are host-dominated, a clear overrepresentation. This is expected since if the pairs of galaxies are interacting objects, the number of starbursts in this subsample of galaxies should consequently increase.

## 5. Conclusions

We present a reliable method of classification of hard X-ray and mid-infrared selected AGN, based on the fit of well-sampled multiwavelength spectral energy distributions with a complete set of AGN and starburst galaxy templates. The sample studied in this paper consists of 96 AGN with unique detection, and 20 AGN with double detection in the EGS. The following results were found:

- Photometric redshifts have been calculated by using the HyperZ code. The measured mean discrepancy between our  $z_{phot}$ 's and a subsample of highly reliable DEEP spectroscopic redshifts (flag = 3 or 4) is  $\Delta z = -0.03$ , with  $\sigma_z = 0.11$ , and 3 outliers (8%). We provide more accurate photometric redshifts than the spectroscopic ones for objects with DEEP flag = 1 or 2.
- Five main population groups have been considered according to the set of templates employed. For the 96 objects in our sample with unique detection, the following percentages have been found: *Starburst-dominated AGN* (24 % of the sample), *Starburst-contaminated AGN* (7 %), *Type-1 AGN* (21 %), *Type-2 AGN* (24 %), and *Normal galaxy hosting AGN* (24 %). We find that 52% of the sample has AGN-dominated SEDs and the remaining 48% host-dominated SEDs.
- 58% of the 96 objects with unique detection in our sample have  $z_{phot} < 1$ , with the rest of the  $z_{phot}$  of the sources distributed in a decreasing tail up to  $z_{phot} = 3$ . The *Starburst-dominated AGN* constitute the high-redshift population of the host-dominated AGN, whilst the *Normal galaxy hosting AGN* are concentrated at low redshifts. In the AGN-dominated group, *Type-1 AGN* are randomly distributed in distance, the *Starburst-contaminated AGN* are located at intermediate values of redshift, and the *Type-2 AGN* are the lowest- $z$  objects.
- An evolutionary trend is noticed, in which the *Starburst-dominated AGN* would be the progenitors of the *Type-1 AGN* and *Type-2 AGN*, via quenching of the starburst through the AGN feedback.

- Correlations between hard/soft X-ray luminosities and ultraviolet/optical/infrared data are reported for such a sample of AGN spanning a wide range of redshift, being in this way represented the behaviour of the different AGN types in the various wavelengths considered.
- *Type-1 AGN* show the highest values of hard and soft X-ray luminosities of the sample, together with the *Starburst-contaminated AGN*, whilst the *Normal galaxy hosting AGN* majority are concentrated at the lowest values, coinciding with the local cool ULIRGs typical hard X-ray luminosities. *Starburst-dominated AGN* and *Type-2 AGN* present intermediate values of X-ray emission, very similar to those of warm ULIRGs. This is consistent with a luminosity-dependent evolution of AGN, with low-luminosity AGN peaking at lower redshifts than luminous active nuclei.
- *Type-1 AGN* are all contained in the IRAC color-color diagram region empirically determined by Stern et al. (2005) for spectroscopically selected AGN. There are many *Type-2 AGN* and *Starburst-dominated AGN* inside this AGN region. These objects have higher mean redshifts than those in the same group but outside the pure-AGN area, according with the evolution of the mid-infrared colors with redshift for star-forming galaxies described in Barmby et al. (2006).
- Mid-infrared  $24\ \mu\text{m}$  to optical  $r$  band flux ratio versus the  $(r-z)_{AB}$  or the  $(r\text{-IRAC } 3.6\ \mu\text{m})_{AB}$  colors show a clear segregation of the different groups in both diagrams. *Starburst-dominated AGN* and *Starburst-contaminated AGN* are displaced towards the highest values of the mid-infrared to optical ratio and display the reddest colors. *Type-1 AGN* and *Type-2 AGN* are located at intermediate values, and the *Normal galaxy hosting AGN* have the lowest values of the  $24\ \mu\text{m}/r$  flux ratio and the bluest colors.
- A tentative classification of objects with double detection into the five main population groups considered through this paper shows an increase of the *Starburst-dominated AGN* of up to 48%, while the others decrease. 61% of the fitted objects show AGN-like SEDs, while 39% is host-dominated.

NASA’s Chandra X-Ray Observatory was launched in July 1999. The Chandra Data Archive (CDA) is part of the Chandra X-Ray Center (CXC) which is operated for NASA by the Smithsonian Astrophysical Observatory.

Based on observations obtained with XMM-Newton, an ESA science mission with instruments and contributions directly funded by ESA Member States and NASA.

GALEX (Galaxy Evolution Explorer) is a NASA Small Explorer, launched in April 2003. We gratefully acknowledge NASA’s support for construction, operation, and science analysis of the GALEX mission, developed in cooperation with the Centre National d’Etudes Spatiales of France and the Korean Ministry of Science and Technology.)

This work is based in part on observations made with the Spitzer Space Telescope, which is operated by the Jet Propulsion Laboratory, California, Institute of Technology under a contract with NASA.

Based on observations obtained with MegaPrime/MegaCam, a joint project of CFHT and CEA/DAPNIA, at the Canada-France-Hawaii Telescope (CFHT) which is operated by the National Research Council (NRC) of Canada, the Institut National des Science de l’Univers of the Centre National de la Recherche Scientifique (CNRS) of France, and the University of Hawaii. This work is based in part on data products produced at TERAPIX and the Canadian Astronomy data Centre as part of the CFHT Legacy Survey, a collaborative project of NRC and CNRS.

Based on observations obtained at the Hale Telescope, Palomar Observatory, as part of a collaborative agreement between the California Institute of Technology, its divisions Caltech Optical Observatories and the Jet Propulsion Laboratory (operated for NASA), and Cornell University.

Many images of this article are based on observations made with the NASA/ESA Hubble Space Telescope, obtained from the data archive at the Space Telescope Science Institute (STScI). STScI is operated by the Association of Universities for Research in Astronomy, Inc., under NASA contract NAS5-26555.

This work uses data obtained with support of the National Science Foundation grants AST 95-29028 and AST 00-71198.

This work is partially funded by PN AYA2007-67965-C03-01, PN AYA2006-02358 and by the Spanish MEC under the Consolider-Ingenio 2010 Program grant CSD2006-00070: First Science with the GTC (<http://www.iac.es/consolider-ingenio-gtc/>). P.G.P.-G. acknowledges support from the Ramón y Cajal Program financed by the Spanish Government and the European Union. C.R.A., J.R.E., G.B., J.G., and P.G.P.-G. acknowledge Roser Pelló, Antonio Cabrera Lavers, and Casiana Muñoz Tuñón for their valuable help. We finally appreciate the very useful report of the anonymous referee.



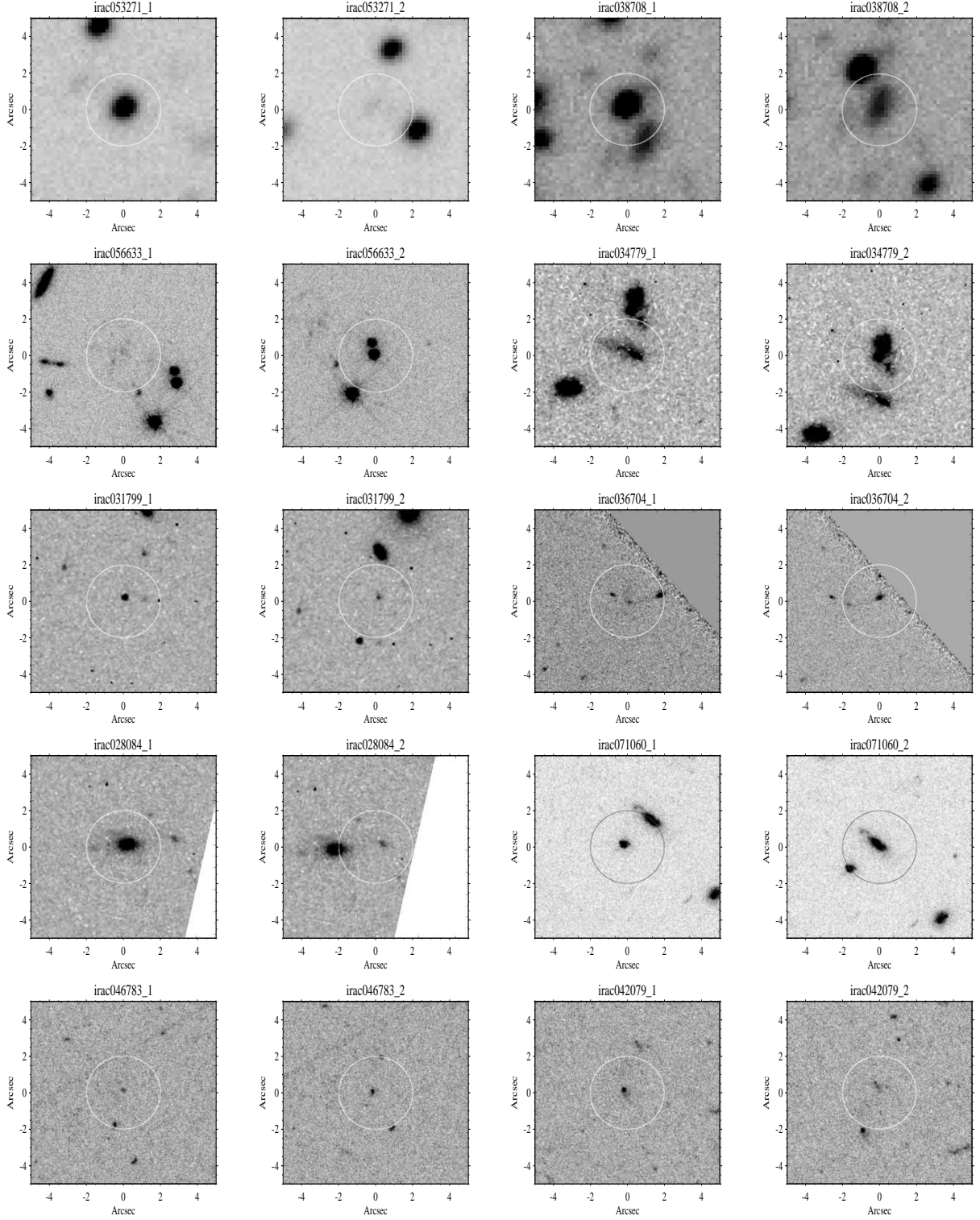


Fig. 7.— Optical images ( $10'' \times 10''$ ) of the sources with double detection in our sample. For objects irac053271 and irac038708, R-band images from CFHTLS are shown. The rest are ACS V-band images: irac056633, irac034779, irac031799, irac036704, irac028084, irac071060, irac046783, and irac042079. Two stamps are shown for each pair of galaxies, the circle indicating the position of each source candidate.



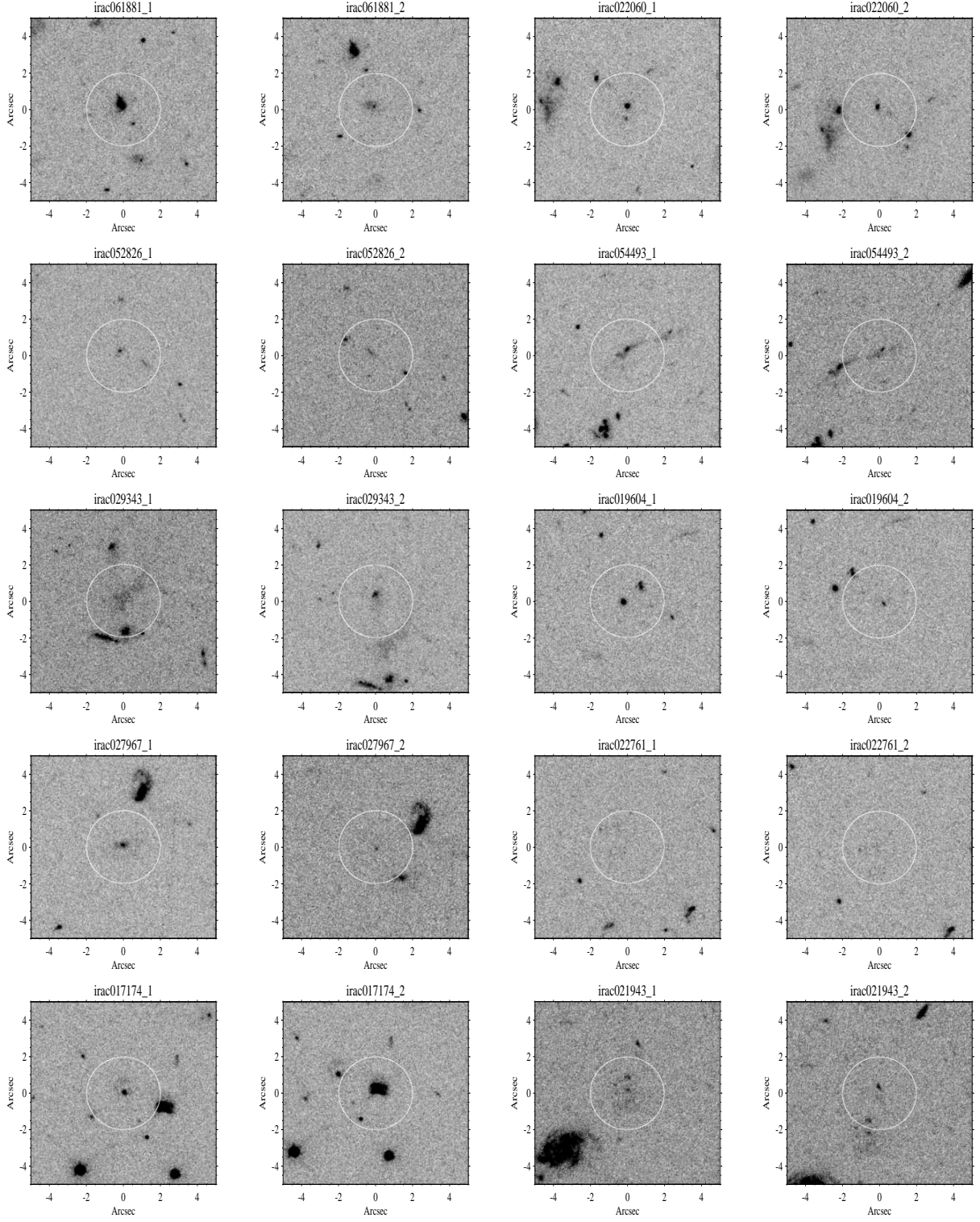


Fig. 8.— Same as in Figure 7 (all the images from ACS V-band/HST), for objects irac061881, irac022060, irac052826, irac054493, irac029343, irac019604, irac27967, irac022761, irac017174, irac021943.

## REFERENCES

- Alexander, D. M., et al. 2003, *AJ*, 125, 383
- Alonso-Herrero, A., et al. 2004, *ApJS*, 154, 155
- Alonso-Herrero, A., et al. 2006, *ApJ*, 640, 167
- Babbedge, T. S. R., et al. 2004, *MNRAS*, 353, 654
- Barger, A. J., Cowie, L. L., Mushotzky, R. F., & Richards, E. A. 2001, *AJ*, 121, 662
- Barger, A. J., Cowie, L. L., Mushotzky, R. F., Yang, Y., Wang, W.-H., Steffen, A. T., & Capak, P. 2005, *AJ*, 129, 578
- Barmby, P., et al. 2006, *ApJ*, 642, 126
- Bolzonella, M., Miralles, J.-M., & Pelló, R. 2000, *A&A*, 363, 476
- Bongiorno, A., et al. 2007, *A&A*, 472, 443
- Boulade, O., et al. 2003, *Proc. SPIE*, 4841, 72
- Brusa, M., et al. 2005, *A&A*, 432, 69
- Brandt, W. N. & Hasinger, G. 2005, *ARA&A*, 43, 827
- Bundy, K., et al. 2006, *ApJ*, 651, 120
- Bundy, K., et al. 2008, *ApJ*, 681, 931
- Calzetti, D. et al. 2000, *ApJ*, 533, 682
- Cardamone, C. N., et al. 2008, *ApJ*, 680, 130
- Cocchia, F., et al. 2007, *A&A*, 466, 31
- Davis, M., et al. 2007, *ApJ*, 660, 1
- Dickinson, M., et al. 2001, *BAAS*, 33, 820
- Donley, J. L., Rieke, G. H., Rigby, J. R., & Pérez-González, P. G. 2005, *ApJ*, 634, 169
- Donley, J. L., Rieke, G. H., Pérez-González, P. G., Rigby, J. R., & Alonso-Herrero, A. 2007, *ApJ*, 660, 167

- Donley, J. L., Rieke, G. H., Pérez-González, P. G., & Barro, G. 2008, *ApJin* press, arXiv:0806.4610
- Dunlop, J. S., McLure, R. J., Kukula, M. J., Baum, S. A., O’Dea, C. P., Hughes, D. H. 2003, *MNRAS*, 340, 1095
- Dye, S. 2008, *MNRASin* press, arXiv:0806.1222
- Eckart, M. E., et al. 2006, *ApJS*, 156, 35
- Eisenhardt, P., et al. 2004, *ApJS*, 154, 48
- Fiore, F., et al. 2003, *A&A*, 409, 79
- Fiore, F., et al. 2008, *ApJ*, 672, 94
- Franceschini, A. et al. 2003, *MNRAS*, 343, 1181
- Franceschini, A. et al. 2005, *AJ*, 129, 2074
- George, I. M., Turner, T. J., Yaqoob, T., Netzer, H., Laor, A., Mushotzky, R. F., Nandra, K., & Takahashi, T. 2000, *ApJ*, 531, 52
- Granato, G. L., De Zotti, G., Silva, L., Bressan, A. & Danese, L. 2004, *ApJ*, 600, 580
- Grogin, N. A., et al. 2005, *ApJ*, 627, 97
- Groth, E. J., et al. 1994, *BAAS*, 26, 1403
- Hasinger, G. 2003a, in "The Emergence of Cosmic Structure", ed. S. S.Holt, & C. S. Reynolds, *AIP Conf. Proc.*, 666, 227
- Hasinger, G. 2003b, in "The restless high energy universe", ed. E. P. J. van den Heuvel, J. J. M. in ’t Zand, and R. A. M. J. Wijers, *Nucl. Physics B. Suppl. Ser.* (astro-ph/0310804)
- , Hasinger, G., Miyaji, T., & Schmidt, M. 2005, *A&A*, 441, 417
- Hatziminaoglou, E., et al. 2005, *AJ*, 129, 1198
- Hornschemeier, A. E., et al. 2001, *ApJ*, 554, 742
- Jannuzi, B. T., & Dey, A. 1999, in *ASP Conf. Ser.* 191, Photometric Redshifts and the Detection of High Redshift Galaxies, ed. R. Weymann et al. (San Francisco: ASP), 11

- Kauffmann, G., et al. 2003, MNRAS, 346, 1055
- Kitsionas, S., Hatziminaoglou, E., Georgakakis, A., & Georgantopoulos, I. 2005, A&A, 434, 475
- Kron, R. G. 1980, ApJS, 43, 305
- Krumpe, M., et al. 2007, A&A, 466, 41
- Kuraszkiewicz, J. K., et al. 2003, ApJ, 590, 128
- Lacy, M., et al. 2004, ApJS, 154, 166
- Lacy, M., Petric, A. O., Sajina, A., Canalizo, G., Storrie-Lombardi, L. J., Armus, L., Fadda, D., & Marleau, F. R. 2007, AJ, 133, 186
- LaFranca, F., Franceschini, A., Cristiani, S., & Vio, R. 1995, A&A, 299, 19
- LaFranca, F., et al. 2005, ApJ, 635, 864
- Lonsdale, C. J., et al. 2003, PASP, 115, 897
- Mainieri, V., et al. 2002, A&A, 393, 425
- Martínez-Sansigre, A., Rawlings, S., Lacy, M., Fadda, D., Marleau, F. R., Simpson, C., Willott, C. J., & Jarvis, M. J. 2005, Nature, 436, 666
- Martínez-Sansigre, A., et al. 2007, MNRAS, 379, L6
- Mushotzky, R. 2004, in Suppermassive Black Holes in the Distant Universe, ed. A. J. Barger (Dordrecht: Kluwer), 53
- Nandra, K., et al. 2005, MNRAS, 356, 568
- Park, S. Q., et al. 2008, ApJ, 678, 744
- Pérez-González, P. G., et al. 2008, ApJ, 675, 234
- Pérez-González, P. G., Trujillo, I., Barro, G., Gallego, J., Zamorano, J., & Conselice, C. J. 2008, ApJ, in press, arXiv:0807.1069
- Pérez-González, P. G., et al. 2005, ApJ, 630, 82
- Peterson, K. C., Gallagher, S. C., Hornschemeier, A. E., Muno, M. P., & Bullard, E. C. 2006, AJ, 131, 133

- Piccinotti, G., Mushotzky, R. F., Boldt, E. A., Holt, S. S., Marshall, F. E., Serlemitsos, P. J., & Shafer, R. A. 1982, *ApJ*, 253, 485
- Pierce, C. M., et al. 2007, *ApJ*, 660, 19
- Polletta, M. et al. 2007, *ApJ*, 663, 81
- Risaliti, G., Maiolino, R., & Salvati, M. 1999, *ApJ*, 522, 157
- Schawinski, K., et al. 2007, *MNRAS*, 382, 1415
- Springel, V., Di Matteo, T., & Hernquist, L. 2005, *MNRAS*, 361, 776
- Steffen, A. T., et al. 2006, *AJ*, 131, 2826
- Steidel, C. C., Adelberger, K. L., Giavalisco, M., Dickinson, M., & Pettini, M. 1999, *ApJ*, 519, 1
- Stern, D., et al. 2005, *ApJ*, 631, 163
- Strateva, I. V., Brandt, W. N., Schneider, D. P., Vanden Berk, D. G., & Vignali, C. 2005, *AJ*, 130, 387
- Szokoly, G. P., et al. 2004, *ApJS*, 155, 271
- Ueda, Y., Akiyama, M., Ohta, K., & Miyaji, T. 2003, *ApJ*, 598, 886
- Vignali, C., Brandt, W. N., & Schneider, D. P. 2003, *AJ*, 125, 433
- Villar, V., et al. 2008, *ApJ*, 677, 169
- Waddington, I., Dunlop, J. S., Peacock, J. A., Windhorst, R. A. 2001, *MNRAS*, 328, 882
- Waskett, T. J., et al. 2003, *MNRAS*, 341, 1217
- Weiner, B. J., et al. 2005, *ApJ*, 620, 595
- Wilkes, B. J., Tananbaum, H., Worrall, D. M., Avni, Y., Oey, M. S., & Flanagan, J. 1994, *ApJS*, 92, 53
- Zezas, A., Alonso-Herrero, A., & Ward, M. J. 2001, *Ap&SS*, 276, 601
- Zheng, W., et al. 2004, *ApJS*, 155, 73

Table 1. ID from Barmby et al. (2006), IRAC ID, IRAC 3.6  $\mu\text{m}$  J2000.0 right ascension and declination, spectroscopic redshift from DEEP public database with its corresponding reliability between brackets (1-2 = low reliability, 3-4= high reliability), photometric redshift and its corresponding  $\chi^2_\nu$  and probability, optical extinction derived from the Calzetti et al. (2000) reddening law, logarithm of  $\nu L_\nu$  in the r band as a reference, in  $\text{erg s}^{-1}$ , fitted template, and main group classification.

Templates: 1,2-Starburst/ULIRG, 3,5-Starburst, 4-Sy1/Starburst/ULIRG, 6-Sy2/Starburst, 13-Sy2/Starburst/ULIRG, 7,12,14-Type-1 QSO, 8-Type-2 QSO, 9-Sy1.8, 10-Sy2, 11-Torus-QSO, 15,16,17-Ellipticals of 2, 5, and 13 Gyr, 18,19,20,21,22,23-Spirals of types S0, Sa, Sb, Sc, Sd, and Sdm.

ID	ID IRAC	RA ( $^\circ$ )	Dec ( $^\circ$ )	$z_{\text{spec}}$	$z_{\text{phot}}$	$\chi^2_\nu$	Prob (%)	$A_V$	$L_r$	Template	Group
1	054396	213.9870	52.2687	-	0.66	0.10	100	0.3	43.80	7	Type-1 AGN
2	067129	214.0352	52.3547	-	0.06	0.06	99	0.0	41.93	15	NG hosting AGN
3	045621	214.0441	52.2727	-	0.25	0.27	98	0.9	43.39	19	NG hosting AGN
4	068644	214.0572	52.3766	1.701 (2)	0.05	1.15	32	0.9	40.55	7	Type-1 AGN
5	056094	214.0591	52.3276	0.534 (4)	0.50	2.51	1	0.0	43.46	22	NG hosting AGN
6	048319	214.0948	52.3212	1.603 (4)	0.76	1.41	18	0.0	44.21	4	SB-cont. AGN
7	019994	214.0956	52.2034	-	1.37	0.48	92	1.2	44.95	14	Type-1 AGN
8	060727	214.1236	52.3925	-	0.96	0.59	81	0.3	44.40	10	Type-2 AGN
9	053898	214.1298	52.3695	-	0.26	2.93	0	0.0	42.71	9	Type-2 AGN
10	040342	214.1367	52.3171	1.028 (4)	0.95	0.83	60	0.0	43.81	4	SB-cont. AGN
14	052726	214.1587	52.3857	0.417 (4)	0.35	0.40	95	0.0	43.98	19	NG hosting AGN
16	059064	214.1765	52.4241	-	0.05	2.26	1	0.3	43.89	15	NG hosting AGN
17	029938	214.1768	52.3034	-	1.06	0.98	45	0.0	45.65	7	Type-1 AGN
20	040860	214.1815	52.3506	0.283 (2)	0.12	0.91	53	0.0	43.20	20	NG hosting AGN
21	045337	214.1832	52.3720	0.510 (4)	0.45	0.38	96	0.0	43.99	20	NG hosting AGN
22	071927	214.1891	52.4850	1.630 (2)	1.55	0.24	99	0.9	44.08	14	Type-1 AGN
24	054089	214.2060	52.4252	-	2.35	0.49	90	0.6	44.75	14	Type-1 AGN
25	019616	214.2065	52.2815	0.761 (4)	0.75	0.62	78	0.3	43.78	22	NG hosting AGN
26	024423	214.2079	52.3025	0.808 (4)	0.73	0.23	99	0.0	43.87	3	SB-dom. AGN
27	017652	214.2104	52.2763	0.683 (4)	0.60	0.29	98	0.9	44.16	6	SB-cont. AGN
29	033772	214.2136	52.3461	-	0.85	1.67	7	0.0	44.70	9	Type-2 AGN
30	058423	214.2163	52.4501	-	0.90	0.27	98	0.3	44.32	10	Type-2 AGN
33	042611	214.2433	52.4036	-	0.90	0.87	53	0.0	42.61	4	SB-cont. AGN
35	021276	214.2529	52.3218	-	0.32	0.15	100	0.3	43.61	9	Type-2 AGN
36	041222	214.2675	52.4149	0.281 (4)	0.25	1.13	33	0.6	43.75	23	NG hosting AGN
38	068074	214.2737	52.5297	0.426 (2)	1.56	1.59	9	0.0	44.13	2	SB-dom. AGN
41	068708	214.2850	52.5403	-	1.36	0.62	80	0.3	44.16	5	SB-dom. AGN
42	056274	214.2862	52.4917	-	1.26	1.17	30	0.6	43.79	2	SB-dom. AGN
43	046787	214.2870	52.4525	0.532 (4)	0.47	0.13	100	0.0	43.90	20	NG hosting AGN
45	050845	214.2940	52.4747	-	1.25	0.99	45	0.3	44.53	1	SB-dom. AGN
47	039386	214.2961	52.4280	-	0.34	0.93	51	0.3	44.00	19	NG hosting AGN
48	062600	214.2984	52.5257	0.835 (4)	0.84	0.87	57	0.0	44.13	21	NG hosting AGN
49	016716	214.2994	52.3366	0.433 (4)	0.45	1.37	18	0.6	44.08	22	NG hosting AGN
50	036500	214.3096	52.4259	-	0.32	0.73	60	1.2	43.59	12	Type-1 AGN
51	071816	214.3118	52.5720	-	1.20	1.38	18	1.2	44.17	2	SB-dom. AGN
52	026610	214.3127	52.3869	1.271 (3)	0.48	0.27	99	0.0	43.41	14	Type-1 AGN
53	041138	214.3134	52.4474	0.723 (4)	0.67	1.08	38	0.0	44.14	9	Type-2 AGN
55	041987	214.3290	52.4623	1.211 (3)	1.23	0.27	98	0.0	44.10	1	SB-dom. AGN
56	042538	214.3303	52.4655	1.208 (3)	1.19	1.35	19	0.0	43.71	10	Type-2 AGN
57	030161	214.3335	52.4168	-	0.88	1.03	42	0.3	44.19	8	Type-2 AGN
59	055009	214.3456	52.5288	0.465 (4)	0.46	0.42	94	0.0	43.52	21	NG hosting AGN
60	055370	214.3475	52.5316	0.484 (4)	0.50	0.29	98	0.0	43.64	9	Type-2 AGN
61	031265	214.3483	52.4320	-	1.19	1.01	43	1.2	44.42	1	SB-dom. AGN
62	057218	214.3510	52.5416	0.902 (4)	0.83	1.39	17	0.0	43.59	3	SB-dom. AGN
63	048619	214.3525	52.5069	0.482 (4)	0.54	1.50	12	0.3	44.49	14	Type-1 AGN
64	069965	214.3553	52.5956	-	1.16	0.18	97	0.0	43.22	4	SB-cont. AGN



Table 1—Continued

ID	ID IRAC	RA ( $^{\circ}$ )	Dec ( $^{\circ}$ )	$z_{spec}$	$z_{phot}$	$\chi^2_{\nu}$	Prob (%)	$A_V$	$L_r$	Template	Group
66	051055	214.3637	52.5254	-	1.57	1.38	18	1.2	43.79	2	SB-dom. AGN
67	068063	214.3704	52.5984	-	1.43	0.85	58	0.3	44.40	3	SB-dom. AGN
69	034221	214.3748	52.4633	-	0.91	0.38	92	0.6	44.50	10	Type-2 AGN
72	035715	214.3784	52.4718	-	1.42	1.19	29	1.2	43.79	2	SB-dom. AGN
73	049420	214.3859	52.5342	0.986 (4)	0.91	0.38	96	0.6	43.87	16	NG hosting AGN
74	055653	214.3909	52.5637	0.551 (4)	0.52	0.39	95	0.3	43.90	22	NG hosting AGN
75	019988	214.3911	52.4155	-	0.92	1.14	33	0.0	43.72	3	SB-dom. AGN
76	044463	214.3932	52.5186	0.271 (4)	0.29	0.42	95	0.6	43.86	16	NG hosting AGN
77	032243	214.3952	52.4696	-	1.73	1.52	11	0.0	45.29	1	SB-dom. AGN
78	040934	214.3998	52.5083	-	2.42	0.61	82	0.3	45.61	14	Type-1 AGN
79	039818	214.4012	52.5047	-	0.93	1.31	21	0.3	42.85	2	SB-dom. AGN
80	061825	214.4014	52.5957	0.197 (1)	2.32	1.56	10	0.0	44.92	1	SB-dom. AGN
81	016037	214.4037	52.4084	-	2.33	1.37	19	0.3	44.79	14	Type-1 AGN
82	062180	214.4043	52.5994	-	0.25	1.22	27	0.0	44.79	22	NG hosting AGN
83	035272	214.4056	52.4893	-	1.19	0.36	87	0.9	43.83	9	Type-2 AGN
84	053837	214.4112	52.5706	-	1.11	1.17	30	0.3	43.65	2	SB-dom. AGN
86	031503	214.4127	52.4789	-	0.90	0.74	69	1.2	43.68	9	Type-2 AGN
87	031796	214.4137	52.4806	-	1.02	0.53	88	0.0	44.32	10	Type-2 AGN
89	057956	214.4228	52.5959	-	1.39	0.37	95	0.0	44.33	10	Type-2 AGN
90	028146	214.4244	52.4732	1.148 (4)	1.15	2.43	1	0.6	44.53	4	SB-cont. AGN
91	031444	214.4393	52.4976	0.873 (4)	0.87	1.27	24	0.9	43.76	1	SB-dom. AGN
92	024070	214.4401	52.4672	0.224 (2)	0.23	0.61	82	0.0	43.03	22	NG hosting AGN
93	033761	214.4415	52.5091	0.985 (3)	0.97	1.95	3	0.6	44.43	8	Type-2 AGN
95	027043	214.4445	52.4829	-	1.78	0.93	50	0.9	43.90	2	SB-dom. AGN
97	024055	214.4460	52.4713	-	2.58	0.27	90	1.2	43.83	12	Type-1 AGN
98	051437	214.4472	52.5862	1.547 (3)	2.37	0.92	51	0.3	43.81	7	Type-1 AGN
99	021585	214.4550	52.4676	0.996 (4)	1.00	0.50	87	0.3	44.65	17	NG hosting AGN
101	035904	214.4575	52.5290	-	2.65	0.47	88	0.9	44.30	2	SB-dom. AGN
105	030608	214.4657	52.5129	-	0.87	0.58	82	0.3	43.69	10	Type-2 AGN
106	022680	214.4684	52.4814	-	1.00	0.57	84	0.6	43.92	9	Type-2 AGN
107	021273	214.4707	52.4775	0.671 (3)	0.60	0.40	95	0.3	43.96	22	NG hosting AGN
108	045400	214.4737	52.5795	0.719 (4)	0.65	0.51	88	0.6	43.77	9	Type-2 AGN
109	028312	214.4748	52.5095	-	1.34	1.06	39	0.3	44.43	8	Type-2 AGN
110	031338	214.4760	52.5232	-	0.65	0.81	61	1.2	43.45	10	Type-2 AGN
111	044246	214.4775	52.5774	0.948 (3)	0.85	0.61	81	0.3	43.99	21	NG hosting AGN
112	047305	214.4803	52.5924	-	2.75	0.34	96	0.3	43.91	12	Type-1 AGN
113	029613	214.4868	52.5235	-	0.50	0.52	88	1.2	42.79	7	Type-1 AGN
116	027980	214.4893	52.5186	-	0.16	0.70	67	0.9	42.79	7	Type-1 AGN
118	029054	214.4956	52.5275	-	0.63	0.15	100	0.6	43.69	9	Type-2 AGN
119	046309	214.5015	52.6030	-	2.45	0.31	93	0.0	43.69	13	SB-cont. AGN
124	041429	214.5082	52.5875	-	1.33	0.19	100	0.6	45.13	14	Type-1 AGN
125	042989	214.5119	52.5965	-	2.05	1.14	33	0.3	43.45	1	SB-dom. AGN
126	044785	214.5191	52.6092	0.387 (1)	1.61	1.88	4	1.2	44.49	7	Type-1 AGN
127	032921	214.5270	52.5662	-	1.30	0.70	71	0.0	45.05	10	Type-2 AGN
128	018428	214.5305	52.5083	-	0.90	0.57	84	0.0	44.35	20	NG hosting AGN
133	024215	214.5679	52.5586	-	2.38	2.28	1	0.6	44.54	2	SB-dom. AGN

Table 1—Continued

ID	ID IRAC	RA ( $^{\circ}$ )	Dec ( $^{\circ}$ )	$z_{spec}$	$z_{phot}$	$\chi^2_{\nu}$	Prob (%)	$A_V$	$L_r$	Template	Group
134	016978	214.5751	52.5340	-	1.32	2.04	3	0.3	43.89	3	SB-dom. AGN
135	022888	214.5841	52.5647	-	0.25	1.36	19	0.6	42.35	7	Type-1 AGN
136	018192	214.5888	52.5485	0.036 (1)	0.05	0.59	81	1.2	40.70	7	Type-1 AGN
137	030219	214.5939	52.6020	-	0.84	0.92	50	1.2	43.51	9	Type-2 AGN

Band	Total fit		SB-dom. AGN		SB-cont. AGN		Type-1 AGN		Type-2 AGN		NG hosting AGN	
	$\alpha$	$r$	$\alpha$	$r$	$\alpha$	$r$	$\alpha$	$r$	$\alpha$	$r$	$\alpha$	$r$
FUV	1.22	0.84	1.05	0.81	1.37	0.94	1.29	0.95	-	-	1.12	0.71
NUV	0.83	0.73	1.08	0.83	0.87	0.87	0.99	0.85	-	-	0.72	0.52
u	0.75	0.73	0.90	0.77	-	-	1.01	0.89	-	-	-	-
g	0.70	0.72	0.79	0.72	1.12	0.80	0.99	0.91	0.76	0.58	-	-
r	0.67	0.71	0.71	0.66	-	-	0.97	0.92	0.71	0.57	-	-
i	0.66	0.73	0.71	0.66	-	-	0.96	0.93	0.64	0.55	0.47	0.58
z	0.67	0.73	0.78	0.74	-	-	0.97	0.93	0.64	0.59	0.48	0.57
J	0.68	0.75	0.82	0.79	-	-	0.97	0.94	0.75	0.62	0.48	0.58
K	0.72	0.78	0.78	0.82	1.25	0.87	0.91	0.92	0.66	0.51	0.62	0.67
IRAC3.6	0.81	0.80	1.01	0.83	1.40	0.88	0.90	0.88	0.67	0.49	0.72	0.66
IRAC4.5	0.87	0.80	1.07	0.82	-	-	0.90	0.86	0.77	0.51	0.82	0.67
IRAC5.8	0.91	0.79	0.96	0.73	1.38	0.84	0.90	0.85	0.81	0.53	0.88	0.65
IRAC8.0	0.93	0.80	0.69	0.64	1.40	0.85	0.92	0.87	0.82	0.56	0.98	0.69
MIPS24	1.02	0.70	-	-	-	-	0.89	0.84	0.87	0.50	1.23	0.67

Band	Total fit		SB-dom. AGN		SB-cont. AGN		Type-1 AGN		Type-2 AGN		NG hosting AGN	
	$\alpha$	$r$	$\alpha$	$r$	$\alpha$	$r$	$\alpha$	$r$	$\alpha$	$r$	$\alpha$	$r$
FUV	1.07	0.83	0.92	0.80	0.92	0.95	1.17	0.95	-	-	0.92	0.63
NUV	0.75	0.74	0.87	0.85	-	-	0.87	0.86	-	-	0.68	0.54
u	0.66	0.73	0.70	0.78	-	-	0.87	0.89	-	-	-	-
g	0.61	0.71	0.64	0.72	-	-	0.85	0.90	-	-	-	-
r	0.58	0.70	-	-	-	-	0.84	0.90	-	-	-	-
i	0.57	0.70	-	-	-	-	0.83	0.91	-	-	0.44	0.58
z	0.57	0.70	-	-	-	-	0.83	0.91	-	-	0.45	0.59
J	0.59	0.72	0.52	0.65	-	-	0.82	0.91	-	-	0.45	0.59
K	0.62	0.76	0.49	0.67	-	-	0.79	0.91	-	-	0.55	0.65
IRAC3.6	0.70	0.79	0.64	0.71	-	-	0.79	0.88	-	-	0.64	0.65
IRAC4.5	0.76	0.79	0.73	0.74	-	-	0.80	0.87	-	-	0.71	0.65
IRAC5.8	0.79	0.77	0.72	0.72	-	-	0.81	0.87	-	-	0.76	0.62
IRAC8.0	0.80	0.77	0.58	0.67	-	-	0.81	0.88	-	-	0.81	0.63
MIPS24	0.87	0.68	0.66	0.61	-	-	0.77	0.84	-	-	1.02	0.61

Table 2: Photometric band considered, fit slope and correlation coefficient  $r$  of the scatter diagrams between the ultraviolet/optical/infrared bands and the hard X-ray (top) and soft X-ray luminosities (bottom) for the total sample and for the *Starburst-dominated AGN*, *Starburst-contaminated AGN*, *Type-1 AGN*, *Type-2 AGN*, and *Normal galaxy hosting AGN* groups. Spearman’s rank correlation tests have been performed for all scatter diagrams. The values reported in Table 2 are indeed significant ( $p < 0.01$ ).

X-ray range	SB-dom. AGN	SB-cont. AGN	Type-1 AGN	Type-2 AGN	NG hosting AGN
Hard	[42,44]	[43,44]	[40,45]	[42,43]	[40,43]
Soft	[41,44]	[42,44]	[39,45]	[41,43]	[40,43]

Table 3: Hard and soft X-ray luminosity ranges (log) for the *Starburst-dominated AGN*, *Starburst-contaminated AGN*, *Type-1 AGN*, *Type-2 AGN*, and *Normal galaxy hosting AGN* groups. Luminosities are not corrected for absorption.

ID	ID IRAC	s1 IR emission	s2 IR emission	comments
11	053271	Dominant	Negligible	s2 diffuse region, s2 probably not AGN
13	038708	Dominant	Dominant	Interacting system
23	056633	Dominant	Dominant	s1 diffuse region with stellar knots, s2 interacting system itself
31	034779	Dominant	Negligible	Interacting system
32	031799	Dominant	Negligible	s1 QSO-like, s2 probably not AGN
34	036704	Dominant	Negligible	s1 interacting system itseft, s2 probably not AGN
37	028084	Dominant	Negligible	s1 face-on disk galaxy, s2 probably not AGN
39	071060	Dominant	Negligible	Interacting system spectroscopically confirmed, s2 probably not AGN
58	046783	Dominant	Dominant	s1 and s2 QSO-like
65	042079	Dominant	Negligible	s2 probably not AGN, s2 diffuse region with stellar knots
88	061881	Dominant	Negligible	s2 probably not AGN, s2 diffuse region with stellar knots
100	022060	Dominant	Negligible	s1 interacting system itself , s2 probably not AGN
102	052826	Dominant	Negligible	s2 probably not AGN, s2 diffuse region with stellar knots
103	054493	Dominant	Negligible	Interacting system, s2 probably not AGN
117	029343	Dominant	Negligible	s1 diffuse region and interacting system itseft, s2 probably not AGN
121	019604	Dominant	Negligible	s1 interacting system itself, s2 probably not AGN
122	027967	Dominant	Negligible	s2 probably not AGN
129	022761	Dominant	Negligible	s1 and s2 optical dropouts, s2 probably not AGN
131	017174	Dominant	Negligible	Minicluseter, s2 probably not AGN
132	021943	Dominant	Negligible	s1 diffuse regions with stellar knots, s2 probably not AGN

Table 4: ID from Barmby et al. (2006), IRAC ID, mid-infrared emission of sources 1 and 2 in each pair of galaxies, and comments based on visual inspection of the objects. Classification of objects as ”probably not AGN” is based on their mid-infrared emission.

Table 5. ID from Barmby et al. (2006), IRAC ID, IRAC 3.6  $\mu\text{m}$  J2000.0 right ascension and declination, spectroscopic redshift from the DEEP public database with its corresponding reliability between brackets (1-2 = low reliability, 3-4= high reliability), photometric redshifts for both blended galaxies when mid-infrared emission comes from both (13,23 and 58) or for the mid-infrared emitter in rest of the cases, and their corresponding  $\chi^2_\nu$ , probabilities, optical extinctions derived from the Calzetti et al. (2000) reddening law, logarithm of  $\nu L_\nu$  in the r band as a reference, in  $\text{erg s}^{-1}$ , fitted templates, and general classification. Templates are the same described in Table 1.

ID	ID IRAC	RA ( $^\circ$ )	Dec ( $^\circ$ )	$z_{\text{spec}}$	$z_{\text{phot}}$	$\chi^2_\nu$	Prob (%)	$A_V$	$L_r$	Template	Group
11	053271_1	214.1439	52.3775	2.089 (2)	2.44	1.29	23	1.20	45.21	14	Type-1 AGN
13	038708_1	214.1499	52.3200	-	1.09	0.94	49	0.00	44.17	1	SB-dom. AGN
13	038708_2	214.1499	52.3200	-	1.10	1.21	28	0.00	44.11	3	SB-dom. AGN
23	056633_1	214.2032	52.4330	-	1.21	0.35	95	0.00	44.30	5	SB-dom. AGN
23	056633_2	214.2032	52.4330	-	0.26	1.73	6	0.30	43.18	22	NG hosting AGN
31	034779_1	214.2239	52.3567	-	0.22	0.91	53	0.90	42.76	10	Type-2 AGN
32	031799_1	214.2246	52.3453	-	2.67	0.67	76	0.30	44.41	12	Type-1 AGN
34	036704_1	214.2506	52.3845	-	1.41	0.42	92	0.30	44.47	21	NG hosting AGN
37	028084_1	214.2677	52.3611	-	0.44	0.89	55	0.90	43.48	10	Type-2 AGN
39	071060_1	214.2738	52.5418	0.170 (2)	2.34	0.80	64	0.30	44.90	7	Type-1 AGN
58	046783_1	214.3350	52.4867	-	1.23	1.85	5	0.60	43.73	2	SB-dom. AGN
58	046783_2	214.3350	52.4867	-	0.92	3.14	0	0.00	42.67	2	SB-dom. AGN
65	042079_1	214.3627	52.4867	-	1.16	2.30	1	0.00	43.69	8	Type-2 AGN
88	061881_1	214.4148	52.6053	-	0.26	1.72	8	0.00	42.22	9	Type-2 AGN
100	022060_1	214.4551	52.4699	0.998 (2)	0.98	0.75	68	0.00	44.13	10	Type-2 AGN
102	052826_1	214.4590	52.6005	-	1.26	0.33	95	0.90	43.61	2	SB-dom. AGN
103	054493_1	214.4620	52.6093	-	2.43	1.79	6	0.60	44.43	12	Type-1 AGN
117	029343_1	214.4923	52.5262	-	1.12	2.09	2	0.00	43.71	2	SB-dom. AGN
121	019604_1	214.5047	52.4950	0.623 (1)	0.14	1.90	4	0.00	41.48	1	SB-dom. AGN
122	027967_1	214.5062	52.5305	-	0.89	1.31	22	0.30	43.85	21	NG hosting AGN
129	022761_1	214.5373	52.5309	-	1.06	0.77	61	1.20	43.19	1	SB-dom. AGN
131	017174_1	214.5545	52.5202	-	1.15	1.04	41	0.30	44.07	3	SB-dom. AGN
132	021943_1	214.5641	52.5466	-	0.98	0.63	77	0.30	43.44	2	SB-dom. AGN